Quantitative morphometric analysis of single gold nanoparticles by optical extinction microscopy : material permittivity and surface damping effects

Quantitative morphometric analysis of single gold nanoparticles by optical extinction microscopy: material permittivity and surface damping effects

Lukas M Payne,[1,2] Francesco Masia,[1,2] Attilio Zilli,[1,3] Wiebke Albrecht,[4] Paola Borri,[1] and Wolfgang Langbein[2,5]
[1)]*Cardiff University School of Biosciences, Museum Avenue, Cardiff CF10 3AX, UK*
[2)]*Cardiff University School of Physics and Astronomy, The Parade, Cardiff CF24 3AA, UK*
[3)]*Department of Physics, Politecnico di Milano – Piazza Leonardo da Vinci 32, 20133 Milano, Italy*
[4)]*EMAT and NANOlab Center of Excellence, University of Antwerp, Groenenborgerlaan 171, B-2020 Antwerp, Belgium*
[5)]*Corresponding author, langbeinww@cardiff.ac.uk*

(Dated: 16 December 2020)

Quantifying the optical extinction cross-section of a plasmonic nanoparticle has recently emerged as a powerful means to characterise the nanoparticle morphologically, i.e. to determine its size and shape, with a precision comparable to electron microscopy, while using a simple optical microscope. In this context, a critical piece of information to solve the inverse problem, namely calculating the particle geometry from the measured cross-section, is the material permittivity. For bulk gold, many datasets have been reported in the literature, raising the question of which one is more adequate to describe specific systems at the nanoscale. Another question is how the nanoparticle interface, not present in the bulk material, is affecting its permittivity. In this work, we have investigated the role of the material permittivities on the morphometric characterisation of defect-free ultra-uniform gold nanospheres of 10 nm and 30 nm diameter, following quantitative analysis of the polarization and spectrally–resolved extinction cross-section on hundreds of individual nanoparticles. The measured cross sections were fitted using an ellipsoid model. By minimizing the fit error, or the variation of the fitted dimensions with color channel selection, the material permittivity dataset and the surface damping parameter g best describing the nanoparticles are found to be the single crystal dataset by Olmon et al.[1] and $g \approx 1$, respectively. The resulting nanoparticles geometries are in good agreement with transmission electron microscopy of the same sample batches, including both 2D projection and tomography.

I. INTRODUCTION

With the increasing employment of nanoscale materials throughout the sciences, it has become an important issue to accurately assess the size and shape of nanoparticles (NPs), whether for research or industrial applications. Credible and robust measurements of these parameters are also critical to comply with regulations. For NPs with dimensions well below the diffraction limit (~ 250 nm) for visible light, the industry standard to accurately determine NP geometries is electron microscopy (EM). However, EM requires complex and expensive instrumentation, and is time-consuming, which is a serious limitation especially when repeated statistical information on NP populations is required, for example for synthesis development and quality control in NP manufacturing.

Notably, there has been increasing research interest in understanding the relationship between the optical properties of NPs, such as absorption and scattering of light, and the NP size and shape, especially for plasmonic nano-systems exhibiting a strong localised surface plasmon resonance (LSPR). Several methods have been reported to directly measure the NP optical scattering cross-section[2–4] σ_{sca}, the absorption cross-section[5–7] σ_{abs}, or their sum, the extinction cross-section[6,8,9] σ_{ext}. A few studies also reported measurements of the real and imaginary parts of the NP polarizability[10,11]. Once these properties are known, by assuming a particular model for the geometry, it is possible to solve the inverse problem, namely calculating the NP geometry from its polarizability. To realize this, the critical piece of connecting information is the complex material permittivity ε. However, ε is typically obtained by performing ellipsometry measurements on surfaces of bulk materials[1,12,13] rather than on NPs. Therefore, discrepancies arise to the effective ε for NPs due to the spatial extension of the excitations responsible for the material polarization, also known as non-local effects[14,15]. These are specifically relevant for metals, where the conduction electron mean free path at room temperature is typically several tens of nanometers[16], and thus comparable to the NP size. The effect of the electrons experiencing an interface is often modelled as an additional damping of the free electron gas in the Drude model, called electron surface scattering[9,17]. This damping depends on the interface structure and the adjacent material, so that in the literature an increase of the damping for interfaces to strongly bound adjacent materials has been called chemical interface damping[18].

The discrepancy between the permittivity measured by ellipsometry on surfaces of bulk materials and the effective permittivity of metallic NPs can lead to inaccuracies in the determination of the geometric properties from the measured optical properties, and vice versa. One would need to account for the discrepancy either through modelling, for example via the addition of a damping term for surface scattering[9,17,18] to the imaginary part of the Drude model for conduction electrons in a solid, or through the use of the dielectric function measured directly from NPs, rather than bulk material. Measurements of the complex permittivity of single gold NPs of 10 nm and 15 nm size have been presented by Stoller et al.[10], revealing that, in particular for gold nanospheres (GNSs) with

LSPR around 530 nm, the measured imaginary part deviates from that of the bulk significantly, for wavelengths λ below 520 nm. However, it should be noted that the NPs used in that work (manufactured by British Biocell, now called BBISolutions) can vary greatly from the assumed spherical or even ellipsoidal shape as we have shown in Ref. 19. Khadir et al.[11] presented a direct measurement of single NP polarizabilities of gold nanospheres of nominal diameter, $D = 100$ nm, and polystyrene beads of $D = 200$ nm, from which one should be able to deduce ε. In this case, the agreement with the measured bulk permittivity using the Johnson and Christy[12] dataset was good, consistent with the rather large size of the NPs, above the mean-free path. In both cases, NP variability and reliance on nominal specifications limit the ability to present an accurate assessment of permittivity from the measured quantities.

Recently, our group published a technique, dubbed the optical nanosizer[19], providing the 3-dimensional (3D) shape and size of NPs, by a comparison between the dipolar Rayleigh–Gans (ellipsoidal) model, and measurements of σ_{ext} with polarization resolution and coarse spectral resolution. It should be noted that measurements of the individual components of σ_{ext}, namely σ_{sca} and σ_{abs}, are not required, as σ_{ext} can be modelled directly as their sum. The method offers the ability to measure hundreds of NPs in a single field of view, with sensitivities below 1 nm^2, corresponding to the cross-section of a $D \approx 2$ nm GNS. Various nominally spherical and rod shaped gold NPs were investigated. The 3D sizes and shapes obtained by the optical measurements on hundreds of NPs were compared with transmission electron microscopy on the same NP batches, including tomography. The optical nanosizer determined the diameter and anisotropy of the NPs with precision around 1 nm, and 10%, respectively, and generally a good agreement was found with the results from the EM analysis.

Notably, one of the examined samples were GNSs with nominal $D = 30$ nm, which exhibit extreme uniformity in both size and shape, with $\hat{D}/D = \pm 4.5\%$, where the overscript $\hat{}$ indicates the standard deviation of the quantity. In this case, comparison to EM revealed a small, but noticeable discrepancy (beyond the error due to noise) between the mean diameters and aspect ratios (ARs) found by the two techniques, the origin of which remained somewhat unexplained in our previous work. Owing to the extreme uniformity of these NPs and the precision of our analysis method, we hypothesize that the observed discrepancy is linked to an incorrect description of the material permittivity. In this work, we have evaluated this hypothesis by changing the model to take into account different material permittivities, according to various datasets available in literature for gold, and by including a surface damping parameter in the Drude damping rate. We applied the revised model to the morphometric analysis of the $D = 30$ nm ultra-uniform gold nanospheres (UGNSs) previously measured, and on a new dataset acquired on nominally $D = 10$ nm UGNSs. A set of metrics were developed, to robustly and consistently quantify the effects of changing the material permittivity and the surface damping parameter across hundreds of NPs. This study clearly identifies an optimum material permittivity dataset, notably different from the widely used Johnson and Christy[12], shedding light on this subtle yet consequential effect.

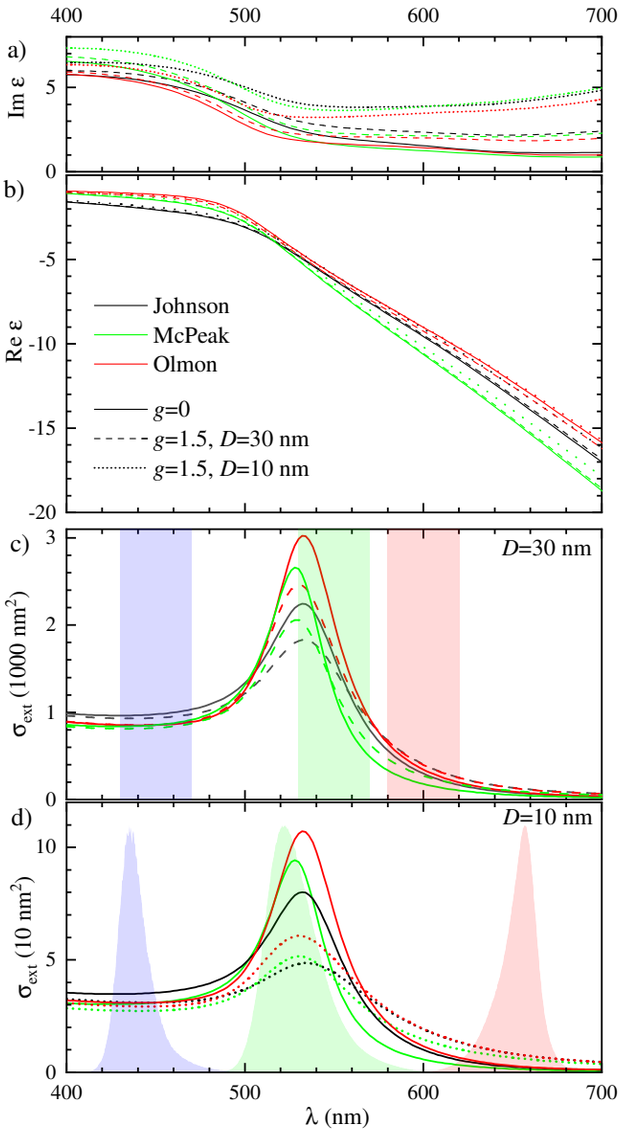

FIG. 1. a),b) Permittivity of gold calculated with the model as discussed in[4,20], fitted to the measured data of Johnson et al.[12], Olmon et al.[1], or McPeak at al.[13], without ($g = 0$) and with strong ($g = 1.5$) surface damping for diameters of $D = 10$ nm and 30 nm. c) Corresponding extinction cross-section of $D = 30$ nm spheres in $n = 1.52$ medium. d) as c) but for $D = 10$ nm. The blue, green and red color bands in (c) represent the passbands of the $\Lambda = (450, 550, 600)$ nm color channels used in the $D = 30$ nm UGNS measurements. The colored spectra in (d) are the LED illumination spectra of $\Lambda = (450, 530, 660)$ nm used in the $D = 10$ nm UGNS measurements.

II. PERMITTIVITY, POLARIZABILITY, AND THE OPTICAL CROSS-SECTIONS OF NANOPARTICLES

The free electron contribution to the complex permittivity in metals is typically calculated using the Drude model. Additionally, bound electron contributions associated with the interband transitions from the d bands into the conduction band are important for gold, since they occur in the visible optical range for $\lambda \lesssim 540\,\mathrm{nm}$, and overlap with the LSPR of spherical NPs. To describe the gold NP permittivity including surface damping, we use here an analytical model[4,20] given by

$$\varepsilon_{\mathrm{NP}} = 1 - \frac{\omega_{\mathrm{p}}^2}{\omega(\omega + i\Gamma)} + \varepsilon^{\mathrm{b}}(\omega), \tag{1}$$

with ω_{p} the plasma frequency, ε^{b} the contribution from the bound electrons[20,21], and Γ the Drude damping rate. To consider surface damping, Γ is approximated[22] by

$$\Gamma = \Gamma_0 + g\frac{v_{\mathrm{F}}}{R}, \tag{2}$$

where $R = D/2$ is the NP radius, Γ_0 is the bulk damping rate, $v_{\mathrm{F}} = 1.4 \times 10^6\,\mathrm{m/s}$ is the Fermi velocity in gold[16], and g is a dimensionless number parameterizing the surface damping. A full set of the parameters used can be found in Table S.1 of Ref. 4. Several experiments have been performed to measure ε of bulk gold. In this work, we refer to those of Johnson & Christy[12], McPeak et al.[13], and Olmon et al[1]. The former two performed spectroscopic ellipsometry on thin polycrystalline films of gold, while Olmon et al. included single crystalline gold. Values of g reported in the literature on gold NPs are varying[9,20] typically between 0.2 and 2, hence we chose to explore this parameter space. For this work, Eq. 1 was used to fit each permittivity dataset independently, for $g = 0$. The resulting models were then evaluated as function of g, providing a series of different $\varepsilon_{\mathrm{NP}}$ to be used to determine the geometric properties of the NPs from the optical measurements. The resulting permittivities are given in Fig. 1a,b, in the absence of surface damping ($g = 0$), and for strong surface damping ($g = 1.5$), for $D = 10\,\mathrm{nm}$ and $30\,\mathrm{nm}$, showing that the surface damping mainly increases the imaginary part of the permittivity $\Gamma\omega_{\mathrm{p}}^2\omega^{-3}/(1+\Gamma^2/\omega^2)$, proportional to the cube of the wavelength for $\Gamma \ll \omega$.

It is relevant at this point to introduce the polarizability, specifically that of the Rayleigh–Gans model, and to formally define the optical cross-sections. The polarizability is determined by the material complex permittivity, the geometry of the NP, and the permittivity, ε_{m}, of the surrounding medium. For an ellipsoidal NP with three semi-axes (a, b, c), we order the semi-axes such that $a \geq b \geq c$, and choose a Cartesian reference system of unit vectors $\vec{e}'_\kappa$, with $\kappa = x'$, y', and z' which point in the directions of a, b, and c respectively. The polarisability tensor $\hat{\alpha}'$ is a diagonal matrix in this basis, whose entries are the polarizabilities for fields oriented along each of the semi-axes of the NP. The diagonal entries are given by

$$\alpha'_j = V\varepsilon_0 \frac{\varepsilon_{\mathrm{NP}} - \varepsilon_{\mathrm{m}}}{\varepsilon_{\mathrm{m}} + L_j(\varepsilon_{\mathrm{NP}} - \varepsilon_{\mathrm{m}})}, \tag{3}$$

with V, the NP volume, ε_0, the free space permittivity, ε_{m}, the dielectric function of the surrounding medium, and L_j, the depolarization factors. The L_j are determined by the geometry of the NP and for a sphere, $L_j = 1/3$. We assume ε_{m} to be real, and constant in frequency, and both NP and medium to be non-magnetic, i.e. having unity relative permeability. For an incident field $\vec{E}'$, we have the induced electric dipole moment,

$$\vec{p}' = \hat{\alpha}'\vec{E}'. \tag{4}$$

For NPs arbitrarily oriented, $\hat{\alpha}'$ must be transformed into the laboratory reference frame, defined by a Cartesian coordinate system with axes labelled $\iota \in \{x, y, z\}$, with unit vectors $\vec{e}_\iota$, where $\vec{e}_z$ points along the optical path, and $\vec{e}_x$, $\vec{e}_y$ span the sample plane. We define[19] the 3D rotation matrix using $\hat{R} = R_\psi R_\theta R_\phi$ and $\hat{R}^\intercal = R_\phi^\intercal R_\theta^\intercal R_\psi^\intercal$, with ϕ, θ, ψ the angles of rotation about $\vec{e}_x$, $\vec{e}_y$, $\vec{e}_z$, respectively. A vector in the NP frame transforms into the laboratory frame as $\vec{v} = \hat{R}\vec{v}'$, so that Eq. 4 becomes $\hat{R}^\intercal\vec{p} = \hat{\alpha}'\hat{R}^\intercal\vec{E}$, and we find that the polarizability in the laboratory frame is

$$\hat{\alpha} = \hat{R}\hat{\alpha}'\hat{R}^\intercal. \tag{5}$$

The optical cross-sections, σ_{sca} and σ_{abs}, are defined as the power scattered P_{sca} or absorbed P_{abs} from the incident field by the NP relative to the intensity, I_{inc}, of the incident field, so that $\sigma_{\mathrm{sca}} = P_{\mathrm{sca}}/I_{\mathrm{inc}}$ and $\sigma_{\mathrm{abs}} = P_{\mathrm{abs}}/I_{\mathrm{inc}}$, respectively. In the electrostatic limit $D \ll \lambda$ the cross-sections are related to $\vec{p}$, and hence $\hat{\alpha}$, via

$$\sigma_{\mathrm{abs}}(\vec{E}) = \frac{k}{\varepsilon_0}\frac{\Im(\vec{E}^* \cdot \vec{p})}{|\vec{E}|^2}, \tag{6}$$

and

$$\sigma_{\mathrm{sca}}(\vec{E}) = \frac{k^4}{6\pi\varepsilon_0^2}\frac{|\vec{p}|^2}{|\vec{E}|^2}, \tag{7}$$

where $k = 2\pi n_{\mathrm{m}}/\lambda$ is the wavenumber in the medium of refractive index, $n_{\mathrm{m}} = \sqrt{\varepsilon_{\mathrm{m}}}$, and the star denotes complex conjugation.

The calculated σ_{ext} for $D = 30\,\mathrm{nm}$ and $D = 10\,\mathrm{nm}$ GNSs ($R = a = b = c = D/2$) are given in Fig. 1 c,d, respectively, for models fitting the three measured permittivities, without surface damping ($g = 0$), or with a strong surface damping ($g = 1.5$). The surface damping is more significant for the smaller GNSs, as follows from Eq. 2, broadening the LSPR, and thus lowering the peak and increasing σ_{ext} at longer wavelengths.

III. EXPERIMENT

The experimental setup and data analysis are described in detail in Ref. 19. We give here a summary and the details relevant to the samples studied in this work.

A. Optical Measurements

The optical transmission measurements were performed using a Nikon Ti-U inverted microscope, with illumination provided by either a 100 W tungsten halogen lamp with bandpass filters (center wavelengths 450 nm, 550 nm, 600 nm) of 40 nm width, or a light emitting diode (LED) source (Thorlabs LED4D106) with 3 independent LEDs of center wavelengths 455 nm, 530 nm, and 660 nm coupled via a liquid light guide (Thorlabs AD5LLG). The excitation spectra are shown in Fig. 1c and d. Light was focused onto the sample with a 1.34 numerical aperture (NA) oil-immersion condenser (Nikon MEL41410), limited to either 0.95 NA or 1.00 NA, and respectively collected by either a 0.95 NA 40× dry objective (Nikon MRD00405) or a 1.45 NA 100× oil objective (Nikon MRD01905), both in conjunction with a 1.5× tube-lens. A linear polarizer before the condenser controlled the excitation polarization angle γ_P. The image data were recorded using a scientific-CMOS (sCMOS) camera (PCO Edge 5.5), capable of acquiring 100 frames per second (FPS) at 2560×2160 pixels and a full well capacity of $N_{\mathrm{fw}} = 30000$ electrons. The illumination intensities and exposure times were chosen to result in pixel values close to N_{fw} without entering the range of non-linear response.

B. Samples and their preparation for optical measurements

NPs branded as 'ultra-uniform GNSs' of nominal spherical shape and mean diameter of 10 nm and 30 nm were obtained from NanoComposix. Glass slides and coverslips (Menzel-Gläser, #1.5) were cleaned by sequential sonication steps in toluene to remove non-polar substances, acetone to clear the toluene, and then rinsed and boiled in deionized (DI) water. Slides and coverslips were then left in 30% hydrogen peroxide for at least 24 hours, allowing oxidation of remaining surface contaminants, as well as hydrophilizing the glass surfaces. It is notable that this protocol offers a reasonable substitute for the much more hazardous 'Piranha' etch, often used to clean glass for similar applications. Prior to NP deposition, any required glass was washed with DI water. The NP colloid was diluted with water to a final concentration of 10^8 NP/ml, and a volume of 200 μl was spin-coated onto the coverslips at 2000 RPM for 2 minutes, with an acceleration time of 30 seconds. This procedure provided a homogeneous density of NPs over the surface of the coverslip of $(0.1-0.4)\,\mathrm{NP}/\mu\mathrm{m}^2$, such that most NPs visible in the image are resolved individuals with well-separated point spread functions (PSFs). The NP side of the coverslip was coated in 18 μl of refractive index $n = 1.52$ silicone oil, and covered with a slide. The samples were pressed, and sealed with clear nail varnish.

C. Measurement of Extinction

We use a method to quantitatively measure σ_{ext}, which has been described in detail in Ref. 23. Briefly, two *brightfield* images called I_1 and I_2 are obtained, differing by a lateral shift of the sample by a few optical resolutions, and averaged over a number, N_{i}, of individual acquisitions, to reduce shot noise. Two extinction images are then obtained as $\Delta_{1,2} = 1 - I_{1,2}/I_{2,1}$. To further reduce shot noise, while simultaneously reducing systematic noise due to sensor electronic drift, we average the extinction over a number of repetitions N_{r}. The extinction cross-section of a NP centred in an area $A_{1,2}$ of radius r_{i} in $I_{1,2}$, is calculated as $2\sigma_{\mathrm{ext}} = \int_{A_1} \Delta_1 \mathrm{d}A + \int_{A_2} \Delta_2 \mathrm{d}A$. The shot-noise-limited standard deviation in the measurement of σ_{ext} is then given by[23]

$$\hat{\sigma}_{\mathrm{ext}} = \frac{r_i d_{\mathrm{px}}}{M} \sqrt{\frac{\pi}{N_{\mathrm{a}} N_{\mathrm{fw}}}}, \tag{8}$$

with the magnification M from sample to detector, the number of acquired frames $N_{\mathrm{a}} = N_{\mathrm{i}} N_{\mathrm{r}}$, and $d_{\mathrm{px}} = 6.5\,\mu$m the pixel pitch of the sensor. We use $r_i = 3\lambda/(2\mathrm{NA})$ unless otherwise stated. For typical values of $N_{\mathrm{i}} = 128$ and $N_{\mathrm{r}} = 4$, $\hat{\sigma}_{\mathrm{ext}}$ is about $50\,\mathrm{nm}^2$, and measurements are shot-noise limited with increasing N_{a} down to $\hat{\sigma}_{\mathrm{ext}}$ of about $4\,\mathrm{nm}^2$. Below this value, surface roughness, debris, and/or residual sensor fluctuations affect the results for our setup and samples. These settings are sufficient for the $D = 30$ nm UGNS which have σ_{ext} in the $10^3\,\mathrm{nm}^2$ range.

For the $D = 10$ nm UGNS, which have σ_{ext} in the few $10\,\mathrm{nm}^2$ range, we instead use a method described in Ref. 23 section IV B, which allows to achieve $\hat{\sigma}_{\mathrm{ext}}$ down to $1\,\mathrm{nm}^2$. Briefly, we reduce the measurement area to the minimum possible, by analyzing Δ_1 via Wiener deconvolution, and hence taking into account the effect of shifted referencing. For $\Delta_1 \ll 1$ the response in the Fourier domain is $h(\vec{k}) = -2i\sin(\vec{k}\cdot\vec{d}/2)$, with $\vec{d}$ the shift vector in real space and $\vec{k}$ the wavevector. The deconvolution is performed by multiplying Δ_1 by $f = 1/[h + 1/(\zeta h^*)]$, with ζ an estimated signal-to-noise ratio (SNR) of the data. We use $\zeta = 1$ and measure the cross-sections directly from the peak values. The pixel values themselves are calibrated in units of σ_{ext} by measuring σ_{ext} of a strong absorber/scatterer with the method mentioned above. Here, we used 60 nm GNSs, added to the sample at lower concentration.

When measuring σ_{ext} as a function of the excitation polarizer angle γ_P, we fit the data with

$$\sigma(\gamma_P) = \sigma\{1 + \alpha\cos[2(\gamma_P - \gamma)]\}, \tag{9}$$

to extract the average given by σ, and the polarisation dependence given by the relative amplitude parameter $\alpha > 0$, and the angle $\gamma \in [0, \pi)$ of maximum σ_{ext}. α is a measure of the observed NP asymmetry, with $\alpha = 0$ corresponding to absence of dipolar asymmetry. γ gives the observed orientation of the NP dipolar asymmetry in the sample plane. We denote the measured extinction cross-section for a certain color channel Λ and polariser orientation γ_P by $\sigma_\Lambda(\gamma_P)$.

D. Structural characterization

Transmission electron microscopy (TEM) was performed on a JEOL-JEM 2100 TEM operating at 200 kV, with sam-

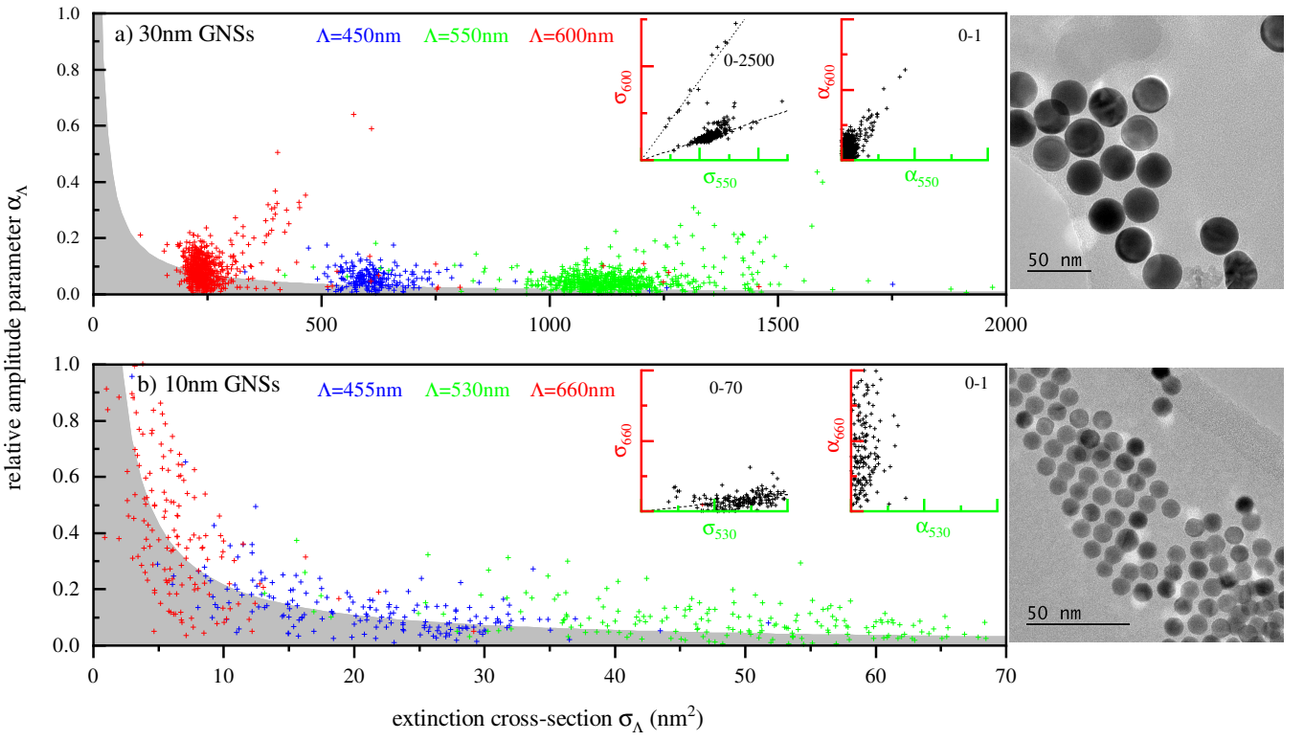

FIG. 2. Asymmetry α_Λ versus cross-section σ_Λ for sets of different NPs and channels Λ as given, with representative TEM images of the investigated NP batch on the right. In all cases, $N_\mathrm{i} = 128$. The grey areas indicate the noise in the fitted α of the red channels due to $\hat{\sigma}_\mathrm{ext}$, estimated as $(\hat{\sigma}_\mathrm{ext}/\sqrt{3})/\sigma_\Lambda$. a) $N = 223$ $D = 30\,\mathrm{nm}$ GNSs using NA $= 0.95$ and $N_\mathrm{r} = (4,4,16)$ for $\Lambda = (450,550,600)$, yielding $\hat{\sigma}_\mathrm{ext} = (57.5, 53.1, 30.9)\mathrm{nm}^2$. Left inset: σ_{600} versus σ_{550}. The dashed line shows $\sigma_{600} = 0.21\sigma_{550}$, and the dotted line $\sigma_{600} = 0.85\sigma_{550}$. Right inset: α_{600} versus α_{550}. Both on a range as indicated. b) $N = 180$ $D = 10\,\mathrm{nm}$ GNSs using NA $= 1.45$ and $N_\mathrm{r} = (16, 16, 46)$ for $\Lambda = (455, 530, 660)$, yielding $\hat{\sigma}_\mathrm{ext} = (4.5, 6.5, 3.7)\mathrm{nm}^2$. Left inset: σ_{660} versus σ_{530}. The dashed line shows $\sigma_{660} = 0.12\sigma_{530}$. Right inset: α_{660} versus α_{530}. Both on a range as indicated. The 30 nm data are also shown in Ref. 19, replicated here for convenience.

ples prepared on 300 mesh hole-y carbon. High-angle annular dark-field scanning transmission electron microscope (HAADF-STEM) images and tomography series were acquired using a FEI Osiris microscope operated at 200 kV. The tomography series were acquired over the tilt range of ±75° with a tilt increment of 3° using a Fischione 2020 single-tilt tomography holder and a pixel dwell time of 6 µs. After alignment of the projection images via a cross–correlation, the stacks of aligned projection images served as inputs for 20 iterations of the expectation maximization reconstruction algorithm implemented in the ASTRA toolbox 1.9.0 using Matlab 2019a[24,25]. Amira 5.4.0 was used for the 3D rendering reported in Fig. 8.

IV. RESULTS AND DISCUSSION

A. Statistical Distributions of σ_Λ and α_Λ

The distribution of α_Λ versus σ_Λ is shown in Fig. 2 for the two UGNS sizes, together with batch-representative TEM images. We call the mean of the polarisation-averaged cross-sections for a given color channel $\bar{\sigma}_\Lambda$, and the associated standard deviation $\hat{\sigma}_{\Lambda,\mathrm{m}}$. The analogous quantities of the α distribution are called $\bar{\alpha}_\Lambda$ and $\hat{\alpha}_{\Lambda,\mathrm{m}}$. For each NP, we determine the error of the fitted parameters σ, α, and γ, using a Monte Carlo-like simulation, as detailed in Ref. 19. Briefly, we add random Gaussian noise to the measured data, matching the experimentally determined noise for each γ_P and Λ, refit the data, and use the standard deviation of the resulting parameter distribution as error. Let us denote the standard deviation of the per-NP fitted parameter σ_i by $\hat{\sigma}_{\Lambda,i}$, where i numbers the N NPs. We then define $\hat{\sigma}_\Lambda = \sqrt{\hat{\sigma}^2_{\Lambda,\mathrm{m}} - \frac{1}{N}\sum_{i=1}^{N}\hat{\sigma}^2_{\Lambda,i}}$, which represents the distribution of NP cross-sections across the various NPs only due to their different sizes and shapes, having subtracted the contribution from measurement noise. Note that for $\hat{\alpha}_{\Lambda,\mathrm{m}}$ this correction has not been done, since the corresponding standard deviations $\hat{\alpha}_{\Lambda,i}$ vary strongly depending on $\hat{\alpha}_{\Lambda,\mathrm{m}}$ and $\bar{\sigma}_\Lambda$, and we use $\hat{\alpha}_\Lambda = \hat{\alpha}_{\Lambda,\mathrm{m}}$.

Fig. 2a presents the measured σ_Λ and α_Λ of a set of $D = 30\,\mathrm{nm}$ UGNSs, which exhibit narrow distributions of both σ_Λ and α_Λ. We find α_{600} to be below 0.2 (apart from some outliers accounting for 4.7% of the population) with a mean and standard deviation $\bar{\alpha}_{600} \pm \hat{\alpha}_{600} = 0.058 \pm 0.031$, indicating NPs of very low ellipticity. $\hat{\sigma}_{450}/\bar{\sigma}_{450}$ and $\hat{\sigma}_{550}/\bar{\sigma}_{550}$ are both about 18%. For NPs much smaller than the wavelength, σ_ext

is roughly proportional to the NP volume V, hence 18% relative volume distribution corresponds to 6% radius distribution. $\hat{\sigma}_{600}/\bar{\sigma}_{600}$ is larger, about 41%, consistent with the fact that the variability of σ_{ext} at a wavelength above the LSPR of a spherical NP is sensitive to deviations from spherical shape, with elliptical shapes resulting in a red-shifted LSPR. This can be seen in the correlation of increasing σ_{600} with α_{600} for the outliers having larger deviations from the spherical shape in Fig. 2a. Notably, correlating σ_{600} with σ_{550} (see inset), two groups can be identified, with different ratios $\sigma_{600}/\sigma_{550}$, identifying two distinct shapes. The ratio 0.21, indicated by the dashed line, is attributed to a close to spherical shape, while the ratio of 0.85, indicated by the dotted line, is consistent[19] with an oblate shape with $c/a \approx 0.7$. Qualitatively, these observations are consistent with TEM (see Fig. 2a right), where most NPs are defect-free, as indicated by the homogeneous contrast in the bright-field TEM images, and have a close to spherical shape, but some contain defects and are clearly non-spherical. We find that $\bar{\sigma}_{550} > \bar{\sigma}_{450} > \bar{\sigma}_{600}$ as expected for spherical gold NPs with a LSPR at $\lambda \approx 530\,\text{nm}$ in a homogeneous environment of $n = 1.52$ refractive index (see Fig. 1c).

Fig. 2b presents the measured σ_Λ and α_Λ of a set of $D = 10\,\text{nm}$ UGNSs. The cross-sections of these NPs are much smaller, in the $50\,\text{nm}^2$ range, so that we used a larger number of repetitions $N_\text{r} = (16, 16, 46)$ for the LED illumination with $\Lambda = (455, 530, 660)\,\text{nm}$, reducing the noise to $\hat{\sigma}_{\text{ext}} = (4.5, 6.5, 3.7)\,\text{nm}^2$. Considering the measured $\bar{\sigma}_\Lambda = (20.4, 47.6, 5.3)\,\text{nm}^2$, the SNR is (4.5, 7.4, 1.4). Notably, for $D = 30\,\text{nm}$ and associated Λ, the SNR is (10.5, 20.8, 8), considerably higher than for the 10 nm UGNSs, despite the larger N_r used in the latter case. For $\Lambda = 530\,\text{nm}$ (the channel having the highest SNR), we find $\bar{\alpha}_{530} \pm \hat{\alpha}_{530} = 0.092 \pm 0.067$, $\hat{\sigma}_{530}/\bar{\sigma}_{530} = 24\%$, and hence, estimate the relative radius distribution to be about $\sim 8\%$, so that these UGNS exhibit slightly broader distributions of both σ_Λ and α_Λ compared to the $D = 30\,\text{nm}$ nanoparticles. The other color channels have a SNR too small for a similar analysis. Correlating σ_{660} with σ_{530} (see left inset), we find that $\sigma_{660} \approx 0.12\sigma_{530}$. The lower factor arises from the 60 nm red-shift of the $\Lambda = 660$ channel compared to $\Lambda = 600$ channel used for the $D = 30\,\text{nm}$ UGNS. Qualitatively, these observations are consistent with TEM, where most of the NPs are defect-free and have a round, slightly faceted shape, while a few NPs contain defects and hence vary from these shapes, as seen for a few red outliers in Fig. 2 b. Note that α_{660} has a significant noise, as indicated by the gray area, so that for most NPs its SNR is less than one, as also seen in the right inset where no correlation between α_{660} and α_{530} is observed.

B. Morphometric analysis

The morphometric analysis method, solving the inverse problem, is discussed in detail in Ref. 19. Briefly, σ_{sca} and σ_{abs} are calculated over a grid in the multidimensional parameter space b/a, c/a, ϕ, θ, ψ, taking into account the illumination intensity spectra of the color channels Λ and the selected permittivity (see Fig. 1). Interpolants are created for σ_{sca} and σ_{abs} from the values on the grid. Then, for each parameter set on the grid, the measured values are compared to the calculated values using the normalized error,

$$S^2 = \frac{1}{N}\sum_{\gamma_\text{P},\Lambda}\left(\frac{\sigma_\Lambda(\gamma_\text{P}) - \sigma_{\text{abs},\Lambda}(\gamma_\text{P}) - \eta\,\sigma_{\text{sca},\Lambda}(\gamma_\text{P})}{\hat{\sigma}_\Lambda(\gamma_\text{P})}\right)^2, \quad (10)$$

where N is the number of measurements in the experiment, and $\hat{\sigma}_\Lambda(\gamma_\text{P})$ is the measurement noise associated with $\sigma_\Lambda(\gamma_\text{P})$. Only a fraction η of σ_{sca} is measured, since the objective collects light from a finite solid angle, and thus some of the light scattered by the NP is collected. For our experimental configuration we calculated $\eta = 0.864$.[19] The right side of Eq. 10 is a fourth-order polynomial in V, so that we can minimize S^2 versus V using the analytical roots of the third-order algebraic equation $\frac{\text{d}}{\text{d}V}S^2 = 0$, to obtain S and V for the specific dataset, and determine a volume-equivalent diameter, $D_V = \sqrt[3]{6V/\pi}$. All points on the grid with S^2 smaller than a certain cutoff are used as initial guesses for a gradient descent using the σ_{sca} and σ_{abs} interpolants. Hence, for every NP under examination, there can be multiple solutions, and we choose the parameter set with the minimum S^2 over all solutions as the one best describing the size, shape and orientation of the NP. Prior knowledge, such as ensemble size specifications from the NP manufacturer, can also be taken into account, and used to apply a penalty according to the variation of the retrieved parameters from the nominal specifications. We perform this operation as a post-fit sorting and selection routine, and use

$$S_\text{c}^2 = S^2 + \frac{1}{3}\sum_{i\in\{D_V,\,b/a,\,c/a\}}\left(\frac{p_i - \bar{p}_i}{\hat{p}_i}\right)^2, \quad (11)$$

with the mean, $\bar{p}_i$, and the variance, $\hat{p}_i$, obtained from TEM for the parameters p_i, $i \in \{D_V, b/a, c/a\}$, to determine the best parameter set as the one with minimum S_c^2.

In this work, we want to examine the effect of ε_{NP} on the fit results. We choose to consider three quantities to act as a figure of merit (FOM) for ε_{NP}. The first follows naturally from the analytical methodology described above. We observe the effect of ε_{NP} on S, specifically calculating

$$\bar{S} = \sqrt{M\{S^2\}}, \quad (12)$$

where $M\{.\}$ indicates that we take the median of the quantity over the N NPs analyzed. Taking the median instead of the mean is more robust to outliers. In Eq. 10, we normalize the difference between the experiment and the model by $\hat{\sigma}_{\text{ext}}(\gamma_\text{P})$, so that for the correct model, we expect $S = 1$. However, since in our case we have for each NP 6 free parameters and 18 measurements ($\sigma_\Lambda(\gamma_\text{P})$ for 6 different γ_P and 3 different Λ), the number of fit parameters is a significant fraction of the number of values to be fitted, thus the parameters will be able to partially fit the noise. In a simple estimation, we expect a value of $S \approx \sqrt{(18-6)/18} \approx 0.81$.

The second FOM is the median of the penalized error,

$$\bar{S}_\text{c} = \sqrt{M\{S_c^2\}}, \quad (13)$$

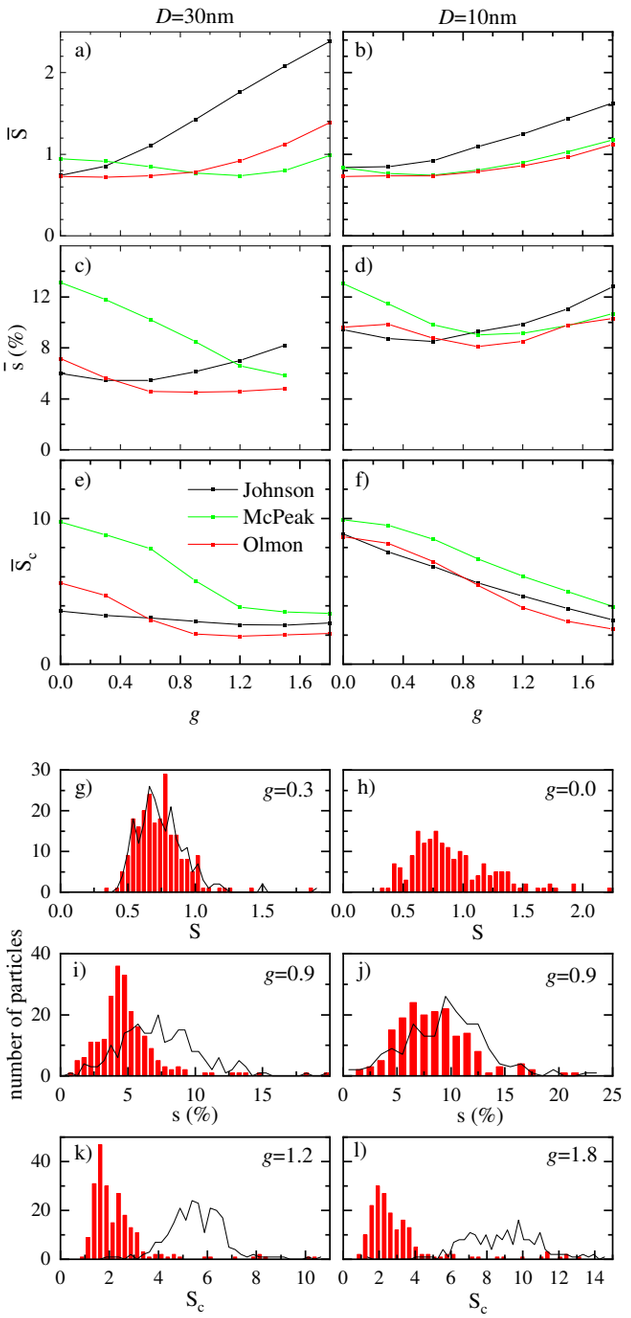

FIG. 3. FOM and statistics for UGNSs of $D = 30\,\text{nm}$ (left column) and $D = 10\,\text{nm}$ (right column). (a,b) $\bar{S}$, (c,d) $\bar{s}$, and (e,f) $\bar{S}_\text{c}$, versus g, with colors indicating the ε dataset used. (g–l) are histograms using the Olmon dataset. (g,h) S with g minimizing $\bar{S}$. The black line shows the case $g = 0$. (i,j) as (g,h) but for s with g minimizing $\bar{s}$. (k,l) as (g,h) but S_c with g minimizing $\bar{S}_\text{c}$.

which takes into account the prior knowledge from TEM, and is a combined agreement with the measurements and the morphology measured by TEM. In contrast to S, the value of S_c can be much larger than 1, in which case it is dominated by the applied penalty. For a correct model and TEM morphology parameters, we expect $\bar{S}_\text{c} \approx \sqrt{2}$, due to the sum of the two normalized variances in Eq. 11.

The third FOM evaluates the consistency of the fitted geometry using different combinations of color channels. Since the wavelength dependence of the model is given mostly by the permittivity, for close-to-spherical NPs, and the NP geometry is independent of wavelength, using the correct permittivity should result in a constant retrieved shape independent of the color channels used, apart from effects of measurement noise. Therefore, the more consistent the NP geometry is between color channel combinations, the better the permittivity describes the NPs.

We have therefore refitted the measured data using each of the three possible combinations of two out of three Λ, which we number with the index $\ell \in \{1,2,3\}$, e.g. for $D = 30\,\text{nm}$ we have $\{450, 550\}\,\text{nm}$, $\{450, 600\}\,\text{nm}$, and $\{550, 600\}\,\text{nm}$. This results in fit parameters $p_{\ell,i}$, for the ℓth Λ combination. We then define the deviation between the fit with the combination ℓ and the fit using all three Λ, as

$$s = \sqrt{\frac{1}{9}\sum_{\ell=1}^{3}\sum_{i\in\{D_V,b/a,c/a\}}\left(\frac{p_{\ell,i}-p_i}{A_i}\right)^2}, \qquad (14)$$

with the normalizing factor $A_i = D_V, 1, 1$, using D_V from the three Λ fit. We define the FOM as median of the s_j over the N NPs,

$$\bar{s} = M\{s\} \qquad (15)$$

providing a measure of the average NP size and shape parameter deviation for fits using two Λ from the one using all three Λ.

The resulting FOMs are shown in Fig. 3 as a function of the surface damping parameter g for each of the experimental ε datasets from Johnson & Christy[12], McPeak et al.[13], and Olmon et al.[1] Looking first at $\bar{S}$, we find that the minimum value is about 0.73, close to the estimated value due to the measurement noise. The lowest values are achieved for the Olmon dataset, for both UGNS sizes. $\bar{S}$ is rather insensitive to the value of g, with a range of 0 to 1 within 10% of the minimum $\bar{S}$. The measurements thus indicate that ε_NP is best described by the Olmon dataset with a surface damping g up to about 1. The histograms of S are shown in Fig. 3(g,h), for Olmon and $g = (0.3, 0.0)$, for which $\bar{S}$ is minimum, and for comparison for $g = 0$ (line). We find a close-to-normal distribution for both sizes, with a weak tail of high S values representing outlier shapes not captured by the model. There is little difference for the two g, consistent with weak dependence of $\bar{S}$ on g.

Next we consider $\bar{s}$, which shows again a minimum for the Olmon dataset, but is more sensitive to g. For $D = 30\,\text{nm}$, there is a minimum at $g = 0.9$, where $\bar{s} = 4.5\%$, and a range within 10% of the $\bar{s}$ minimum for g between 0.5 and 1.5. For $D = 10\,\text{nm}$, the situation is similar, with a minimum at $g = 0.9$, where $\bar{s} = 7.8\%$, and a range within 10% of the minimum for g between 0.6 and 1.3. The larger minimum value of $\bar{s}$ is attributed to the lower SNR for the $D = 10\,\text{nm}$ measurements, providing a less precise retrieval of size and shape, specifically for the two-channel results. Importantly, the results of

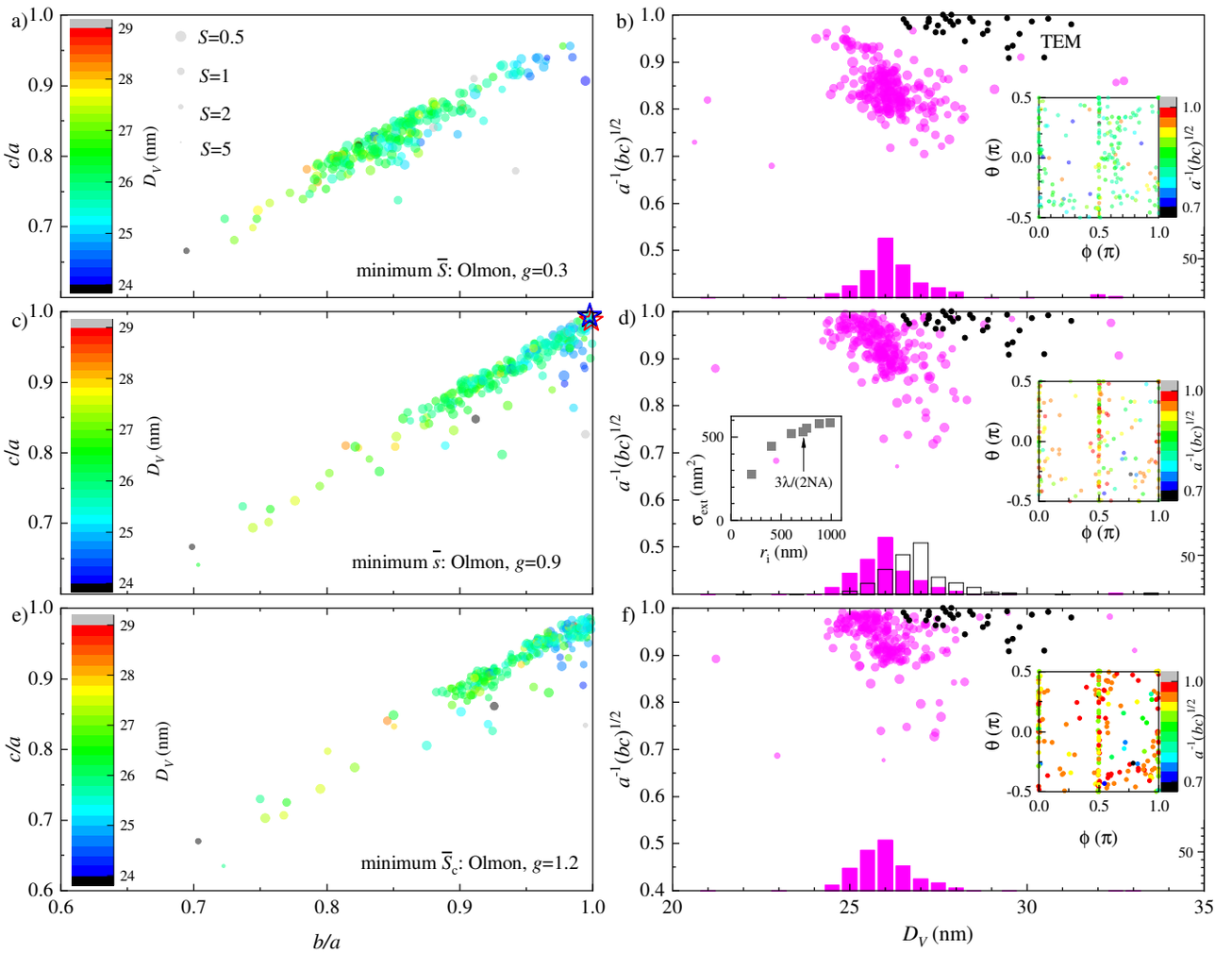

FIG. 4. Fit results for $N = 223$ $D = 30$ nm UGNSs when using (a, b) Olmon with $g = 0.3$ minimizing $\bar{S}$, (c, d) Olmon with $g = 0.9$ minimizing $\bar{s}$, and (e, f) Olmon $g = 1.2$ minimizing $\bar{S}_c$. The left column shows the ARs with a color indicating the fitted diameter D_V. The right column shows the average AR parameter $\sqrt{bc}/a$ as a function of D_V, with the histogram showing the number distribution of D_V. The black points indicate TEM measurements, where we have assumed $b = c$. Insets indicate the pitch (θ) and roll (ϕ) angles determined from the fit, to show the out of plane orientation (ϕ, $\theta \neq 0$). The size of the fit datapoints in (a–f) is given by $S^- = 1/(1+S)$, and represents the fit error with larger points indicating lower error. In (d), an additional retrieved histogram of D_V is shown as black outline bars, resulting when correcting the measured σ_{ext} by a factor 1.105, compensating the finite $r_i = 3\lambda/(2\mathrm{NA})$ used in the analysis. The dependence of the measured σ_{ext} on r_i for $\Lambda = 450$ averaged over 39 NPs is shown in the left inset.

$\bar{s}$ and $\bar{S}$ are compatible, and indicate that for both sizes ε_{NP} is described well by the Olmon dataset with $g = 0.9$. Comparing the different datasets, we see that for $D = 30$ nm the dependence $\bar{S}(g)$ for Johnson is similar to $\bar{S}(g+1)$ for Olmon. Considering that Johnson refers to polycrystalline films, while Olmon to monocrystalline, it appears that the difference can be attributed to the additional surface damping by a crystallite size on the order of 30 nm. McPeak instead shows results less compatible between $\bar{S}$ and $\bar{s}$, and between the two UGNS sizes. It features a stronger Drude contribution, as can be seen in the steeper slope of Re ε towards longer wavelength in Fig. 1b, and in the higher plasma frequency in the model parameters (see Ref. 4 Table S1).

The histograms of s are shown in Fig. 3(i,j), for Olmon and $g = 0.9$, for which $\bar{s}$ is minimum, and for comparison for $g = 0$ (line). We find a rather broad distribution for both UGNS sizes, again with a weak tail of high s values representing outlier shapes not captured by the model. In contrast to the histograms of S, there is a significant difference for the two g, consistent with the stronger dependence of $\bar{s}$ on g. The broad distribution is attributed to the sensitivity of the cross-sections to variations of the shape parameters, as shown in Ref. 19.

Finally, we consider $\bar{S}_c$ which is the only FOM where prior knowledge on the size and shape distribution is used. We find again that the Olmon dataset is the best suited one. For $D = 30$ nm, there is a minimum at $g = 1.2$, where $\bar{S}_c$ is about

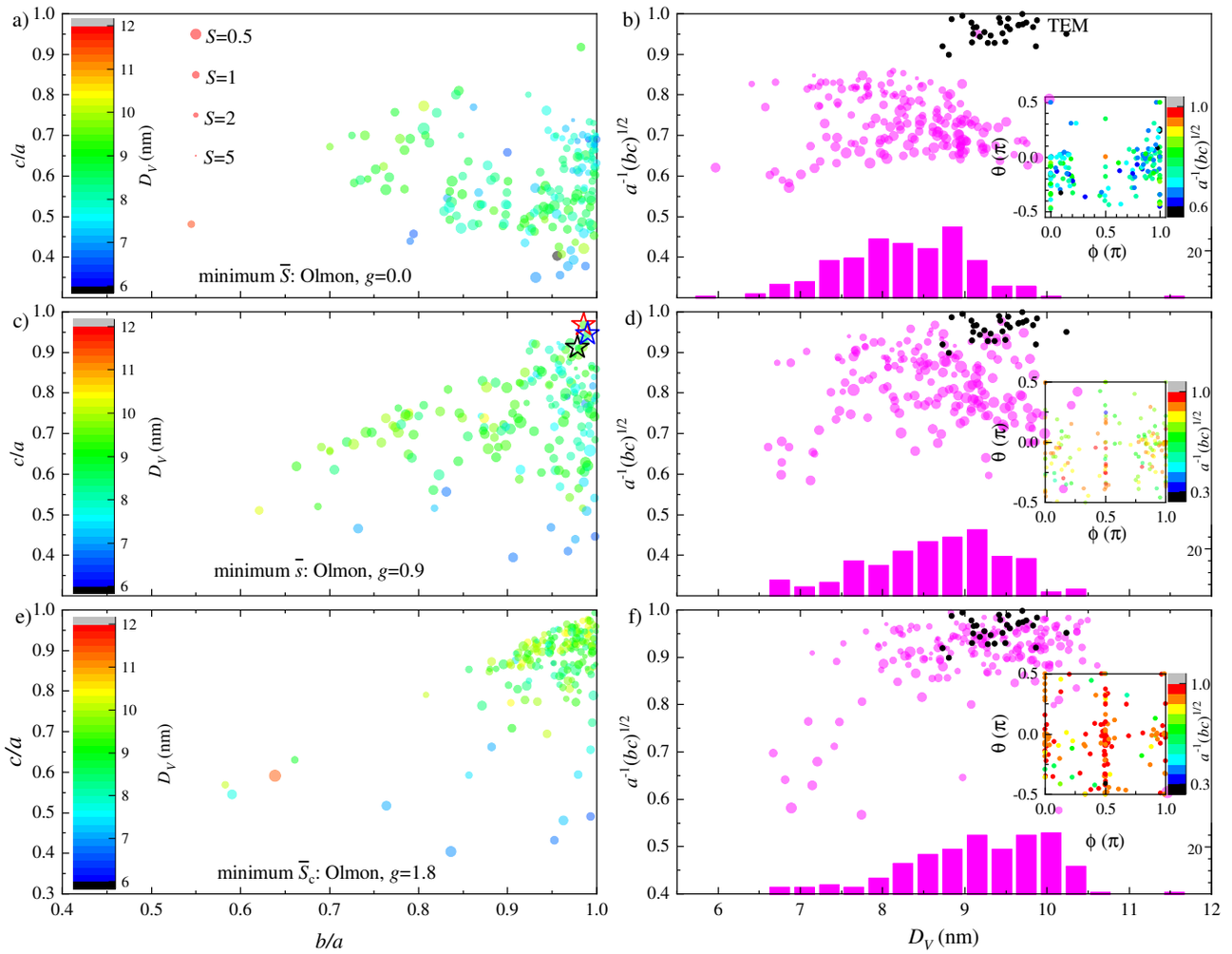

FIG. 5. As Fig. 4, but for $N = 179$ $D = 10$ nm UGNS using (a,b) Olmon $g = 0.3$ minimizing $\bar{S}$, (c,d) Olmon $g = 0.9$ minimizing $\bar{s}$, (e,f) and Olmon $g = 1.8$ minimizing $\bar{S}_c$.

1.9, and a range within 10% of the minimum for g between 0.8 and 1.8. This result is compatible with the one of $\bar{s}$ and $\bar{S}$, indicating that the ellipsoidal model is well suited to describe most of the NP shapes. For $D = 10$ nm however, the minimum occurs for $g \geq 1.8$, deviating significantly from the range given by $\bar{S}$ and $\bar{s}$. This finding is attributed to the lower SNR in these data, resulting in systematic errors in the retrieved shape due to the intricate dependence of the simulated cross-sections on the shape parameters, as will be detailed below.

The optimum value of the surface damping g around 1 found in the present work is consistent with previous reports[4,17] on NPs . In view of the influence of the surface chemistry on g reported in Ref. 18 it is worthwhile to mention that, in the investigated UGNSs, PEG-carboxyl is covalently bound to the surface of the NPs.

In Fig. 4, we show the results of the morphometric fit for the individual NPs, in the case of $D = 30$ nm UGNSs, for the Olmon dataset and g minimizing $\bar{s}$, $\bar{S}_c$, or $\bar{S}_c$. We find that most retrieved NPs shapes are prolate, seen in the left column by the clustering close to the diagonal $a > b \approx c$. For $g = 0.3$ minimizing $\bar{S}$, the averaged AR $\sqrt{bc}/a$ is around 0.82 (see Fig. 4b), while for $g = 0.9$ minimizing $\bar{s}$, this increases to about 0.9 (see Fig. 4d), and for $g = 1.2$ minimizing $\bar{S}_c$, it does not change significantly. Notably, the higher AR is compatible with the TEM data. The angle distributions (see inset in right column) are rather similar for the three values of g.

There is still a small systematic deviation between the diameter D_V determined by the optical sizing and the one seen in TEM (solid circles in Fig. 4d), with the former about 2–3 nm smaller on average. Importantly, the noise in the data is not creating a systematic error in D_V, as demonstrated in Ref. 19 Fig. 6. Therefore this deviation should be attributed to systematic errors in the measurement or the modelling. A known systematics in the evaluation of the cross-section is the usage of a finite area, not completely capturing σ_{ext}. We have discussed this in Ref. 23 – using a smaller area improves the SNR and allows measuring denser NP arrangements. We have analyzed the dependence of σ_{ext} on r_i for $\Lambda = 450$, average over 39 NPs

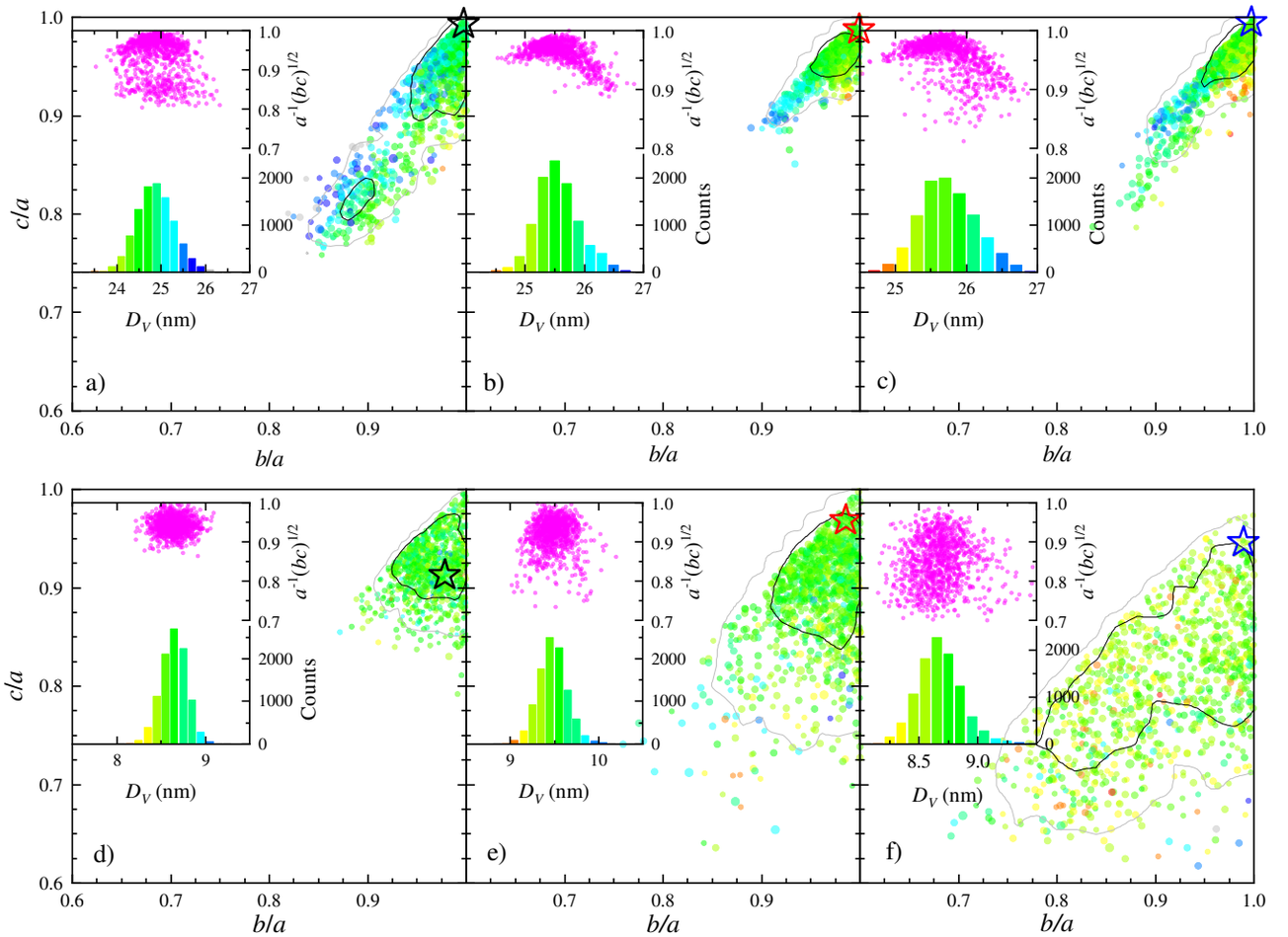

FIG. 6. For the measured NPs indicated by stars in Fig. 5c and 4c, fit results for 10000 realizations (1000 shown by filled circles) of added random measurement noise, using the Olmon dataset with $g = 0.9$. Contours are the boundaries of regions of highest density containing 68% (black) and 95% (grey) of the data. Insets show the distributions of D_V, and provide the symbol color scale, and the AR (magenta). The NPs of the 30 nm UGNS in panels (a,b,c) have $\alpha_{550} = (0.016, 0.033, 0.023)$ and $\sigma_{550} = (1166, 1223, 1233)\,\mathrm{nm}^2$, and the NPs of the 10 nm UGNS in (d,e,f) have $\alpha_{530} = (0.049, 0.025, 0.128)$ and $\sigma_{530} = (57.3, 61.7, 46.0)\,\mathrm{nm}^2$.

which had sufficient separation from other NPs, as shown in the left inset of Fig. 4d. We find a factor of 1.105 between $r_\mathrm{i} = 742\,\mathrm{nm} \approx 3\lambda/(2\mathrm{NA})$, and the maximum $r_\mathrm{i} = 979\,\mathrm{nm}$ analyzed, limited by the lateral shift used in the measurements. The dependence on r_i appears to saturate at this value. Taking this factor into account, the resulting D_V histogram (given in Fig. 4d as black outline) exhibits an increase of the D_V from $(26.0 \pm 1.1)\,\mathrm{nm}$ to $(26.9 \pm 1.1)\,\mathrm{nm}$, consistent with the volume scaling of σ_ext. This reduces the systematic deviation to 1–2 nm, smaller than size distribution. This is a remarkable accuracy given that it depends on the theoretical model and the measurement of the absolute cross-sections.

In Fig. 5 the results for the $D = 10\,\mathrm{nm}$ UGNSs are shown. We find that the retrieved NP shape is more broadly distributed in both b/a and c/a, as well as in diameter. These broadened distributions are mostly related to the measurement noise. For $g = 0.0$ minimizing $\bar{S}$, the shape tends to be more oblate, with ARs spread between 0.6 and 0.9. For $g = 0.9$ minimizing $\bar{s}$, a random ellipsoidal shape is found, with ARs spread between 0.7 and 1.0. The diameter D_V is spread between 7 and 10 nm, which is not dominated by the measurement noise, as we will see below. For $g = 1.8$ minimizing $\bar{S}_\mathrm{c}$, the ARs are pushed towards the spherical shape, more consistent with the TEM data, as expected for this FOM. Notably, the large g results in higher cross-sections for $\Lambda = 660$, so that the fit is biased to avoid non-spherical shapes which would further increase this cross-section.

Unlike the retrieved size D_V, the shape does acquire a significant systematic error due to measurement noise for close-to-spherical NPs, as was demonstrated in Ref. 19 Fig. 6. Indeed, the spherical shape is at the corner of the two-dimensional shape parameter space $1 \geq b/a \geq c/a > 0$, and any noise can only result in non-sphericity. To evaluate the effect in the present data, three close-to-spherical NPs were selected from each of the 10 nm and 30 nm UGNS, indicated by stars in Fig. 5c and Fig. 4c. Random Gaussian noise of

standard deviation $\hat{\sigma}_{\text{ext}}$ was added to the experimental data, and the NP parameters were retrieved from the resulting data using the Olmon dataset with $g = 0.9$. This was repeated for 10000 noise realizations, and the results are shown in Fig. 6. The contours indicate the regions of highest probability density containing 68% and 95% of the data, which for a Gaussian distribution are the σ and 2σ confidence intervals, respectively.

The results for the 30 nm UGNSs in Fig. 6a–c show that the measurement noise results in about 1 nm full-width-at-half maximum (FWHM) in D_V, which is about half the width of the distribution seen in Fig. 4d. The retrieved D_V distribution is thus affected by the noise, but still represents the NP size distribution well. Looking at the shape parameters b/a and c/a, the different NPs shows quite different results. Fig. 6a shows a bimodal distribution, with a maximum close to spherical, and a smaller peak around $b/a = 0.9$ and $c/a = 0.82$. Such multimodal distributions arise from the complex fitting landscape over NP rotation and shape[19]. In Fig. 6b instead the shape is close to spherical, with $b/a \approx 0.97$ and $c/a \approx 0.95$. Finally, in Fig. 6c shows a distribution intermediate between the one in (a) and (c). The measured shape distribution (Fig. 4c,d) is therefore strongly influenced by the measurement noise. While NPs with retrieved ARs below 0.8 cannot be explained by the noise and thus are certainly non-spherical, the majority of the NPs have retrieved ARs above 0.9 and would be consistent with a spherical shape within the measurement noise.

For the 10 nm UGNSs shown in Fig. 6d–f the noise results in about 0.5 nm FWHM in D_V, which is well below the width of the distribution of about 2 nm FWHM seen in Fig. 5d. The width of the NP distribution is therefore not significantly influenced by the noise. Also here, the three selected NPs show different shape distributions, generally more widely spread due to the lower SNR of the data. The shape is spread between spherical and $b/a \gtrsim 0.85$ and $c/a \gtrsim 0.7$, and an AR above 0.8. The measured shape distribution (Fig. 5c,d) is therefore significantly influenced by the measurement noise – however, NPs having a retrieved AR below 0.75 cannot be explained by the noise and thus are non-spherical.

C. Tomography

Tomography was performed on the UGNSs to characterize the morphology of the NPs. Examples of two $D = 30$ nm and three $D = 10$ nm UGNSs, shown in Fig. 8, exhibit largely defect-free (as established from the STEM images used for the reconstruction, see as example Fig. 7), and show faceting. ARs determined from both the 2D projection and the 3D reconstruction are close to one for all five UGNSs. The statistics resulting from HAADF-STEM measurements of 61 $D = 30$ nm and 126 $D = 10$ nm UGNSs are shown in Table II. Both species are highly monodisperse in both D and AR, with $\hat{D}/\bar{D} = 6.3\%$ and $\hat{AR}/\bar{AR} = 2.4\%$ for the $D = 30$ nm NPs, and $\hat{D}/\bar{D} = 3.76\%$ and $\hat{AR}/\bar{AR} = 2.94\%$ for the $D = 10$ nm NPs. This can be compared with the corresponding results from the optical characterization, $\hat{D}_V/\bar{D}_V = 5.1\%$ for the 30 nm and $\hat{D}_V/\bar{D}_V = 22\%$ for the 10 nm UGNSs. While the 30 nm result is consistent with tomography, the 10 nm result shows a much larger size distribution. The measurement noise corresponds to about 1% for the 30 nm and 3% for the 10 nm UGNSs, and is not dominating the findings. Since the STEM statistics was taken not using tomography, there is a possibility that some of the 10 nm UGNSs are flattened, not visible in plan-view STEM but in the optical measurements. Another aspect to be considered is that faceting of NPs depends on their environment, so might change between vacuum (TEM) and oil (optical measurements). For these small NPs the surface facets (see Fig. 7) might have a significant influence on the optical response. Additionally, electron beam induced reshaping might also play a role.

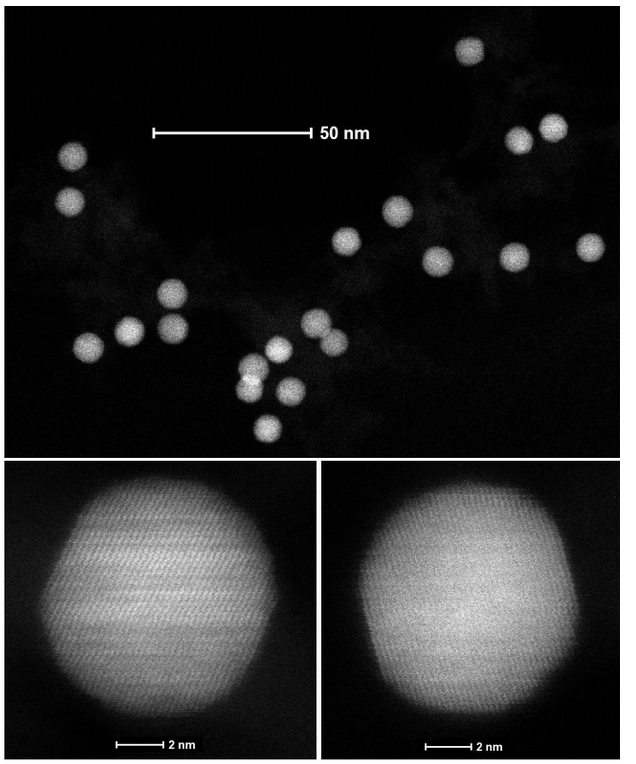

FIG. 7. STEM images of $D = 10$ nm UGNSs

TABLE I. Measured NP volume and AR for the NPs from Fig. 8. A comparison is made between the measured ARs obtained from the 3D reconstruction and the corresponding 2D projection image of the same NP. The ARs were calculated by dividing the length of two orthogonal lines through the middle orthoslice (3D) or the projection image (2D).

NP	Volume (10^3 nm^3)	AR from 3D	AR from 2D
30nm - 1	13.10	0.99	0.98
30nm - 2	12.10	0.96	1.00
10nm - 1	0.472	1.00	1.00
10nm - 2	0.492	0.99	0.99
10nm - 3	0.491	0.98	0.94

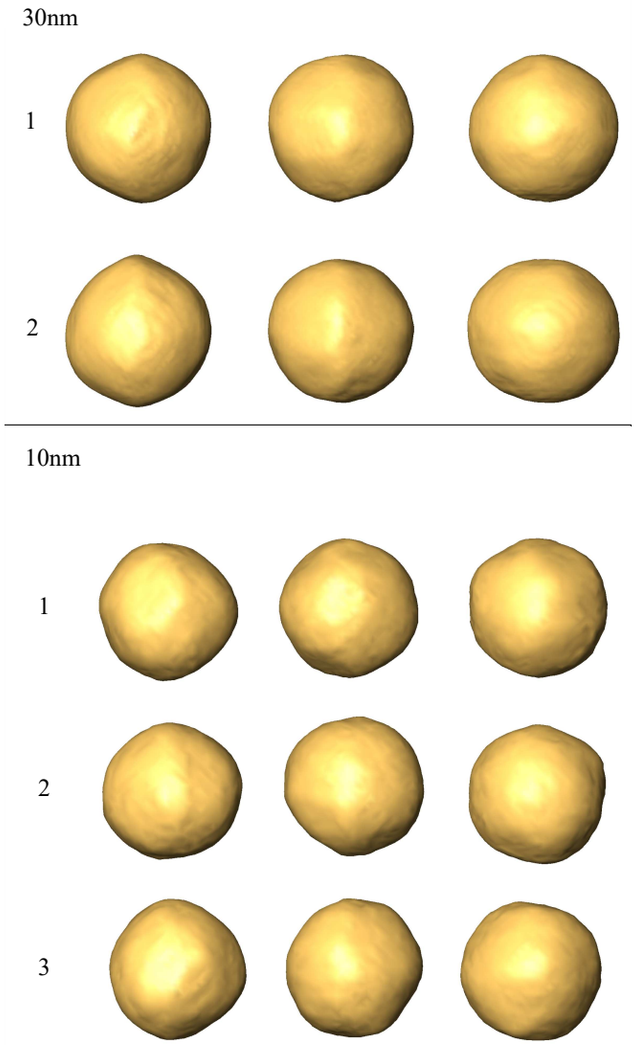

FIG. 8. 3D tomographic reconstructions of two $D = 30\,\text{nm}$ UGNSs (top)[19] and three $D = 10\,\text{nm}$ UGNS (bottom). Each NP is visualized over the same three planes (*xy*, *xz*, and *yz*). The volumes and ARs of each NP can be found in Table I.

TABLE II. HAADF-STEM derived mean and standard deviation of parameters p_i. Here we consider the two main semi-axes seen in the 2D projection, and assign the longer to a, and the shorter to b and c.

NP type	$\bar{p}_{Dv} \pm \hat{p}_{Dv}$(nm)	$\bar{p}_{b/a} \pm \hat{p}_{b/a}$
$D = 30\,\text{nm}$	28.73 ± 1.81	0.973 ± 0.024
$D = 10\,\text{nm}$	9.556 ± 0.359	0.962 ± 0.031

V. CONCLUSIONS

In summary, we have reported an in-depth quantitative analysis of the effects of using three gold permittivity datasets from the literature, and a surface damping parameter varying from 0 to 1.8, when fitting experimentally measured optical extinction cross-sections of hundreds of individual gold nanoparticles. Quantitative measurements of the cross-section magnitude were performed as a function of the incident light polarisation direction, and for 3 colour channels. The samples investigated were ultra-uniform, mostly defect-free, nominally spherical NPs of 30 nm and 10 nm diameter, exhibiting a very narrow size and shape distribution, which enabled us to unravel the effects of permittivity and surface damping, without being affected by the dispersity of the sample. To determine the permittivity dataset and damping parameters best reproducing the measured cross-sections, consistently across hundreds on NPs, we introduced three figure of merits, namely i) the median of the fit error across the population of NPs analysed, ii) the median of a so-called penalised error, using prior knowledge of the NP morphometric parameters from TEM, and iii) the average size and shape parameter deviation for fits using two wavelength combinations compared to three. The smallest FOM was found consistently when using the gold permittivity dataset published by Olmon et al.[1], rather than the widely used Johnson and Christy[12]. The dependence of the FOMs on the damping parameter indicated that $g \approx 1$ describes the data across both sizes. Nanoparticle sizes and shapes obtained by solving the inverse problem with this permittivity compared well with in-plane TEM and tomography analysis, taking into account the measurement precision and accuracy. This study exemplifies the capabilities of optical studies for morphological and compositional analysis of NPs, providing an alternative tool complementing electron microscopy.

ACKNOWLEDGMENTS

This work was supported by a Welsh Government Life Sciences Bridging Fund (grant LSBF/R6-005) the UK EPSRC (grant n. EP/I005072/1 and EP/M028313/1), and by the European Commission (EUSMI E191000350). PB acknowledges the Royal Society for her Wolfson research merit award (grant WM140077). WA acknowledges an Individual Fellowship from the Marie Sklodowska-Curie actions (MSCA) under the EU's Horizon 2020 program (Grant 797153, SOPMEN), and Sara Bals for supporting the STEM measurements. The bright-field TEM was performed by Thomas Davies at Cardiff University. We acknowledge Iestyn Pope for technical support of the optical equipment.

AUTHOR CONTRIBUTION

L.P., W.L. and P.B. conceived the work. L.P. prepared the samples for the optical measurements and performed the related measurements and data analysis. W.A. prepared the samples for the STEM tomography, and performed the related measurements and data analysis. L.P, P.B. and W.L. developed the numerical model and fitting methods. L.P. performed the numerical simulations and data fitting. F.M. calculated the modified permittivity data sets. A.Z. calculated the relative field strengths in the illumination. All authors contributed to

the data interpretation and writing of the manuscript.

DATA AVAILABILITY

Information on the data underpinning the results presented here, including how to access them, can be found in the Cardiff University data catalogue at http://doi.org/10.17035/d.2020.xxx.

[1]R. L. Olmon, B. Slovick, T. W. Johnson, D. Shelton, S.-H. Oh, G. D. Boreman, and M. B. Raschke, "Optical dielectric function of gold," Phys. Rev. B **86**, 235147 (2012).
[2]A. Crut, P. Maioli, N. D. Fatti, and F. Vallée, "Optical absorption and scattering spectroscopies of single nano-objects," Chem. Soc. Rev. **43**, 3921–3956 (2014).
[3]L. M. Payne, W. Langbein, and P. Borri, "Polarization-resolved extinction and scattering cross-section of individual gold nanoparticles measured by wide-field microscopy on a large ensemble," Appl. Phys. Lett. **102**, 131107 (2013).
[4]A. Zilli, W. Langbein, and P. Borri, "Quantitative measurement of the optical cross sections of single nano-objects by correlative transmission and scattering microspectroscopy," ACS Photonics **6**, 2149–2160 (2019).
[5]D. Boyer, P. Tamarat, A. Maali, B. Lounis, and M. Orrit, "Photothermal imaging of nanometer-sized metal particles among scatterers," Science **297**, 1160–1163 (2002).
[6]M. Husnik, S. Linden, R. Diehl, J. Niegemann, K. Busch, and M. Wegener, "Quantitative experimental determination of scattering and absorption cross-section spectra of individual optical metallic nanoantennas," Phys. Rev. Lett. **109**, 233902 (2012).
[7]A. Tcherniak, J. Ha, S. Dominguez-Medina, L. Slaughter, and S. Link, "Probing a century old prediction one plasmonic particle at a time," Nano Lett. **10**, 1398–1404 (2010).
[8]A. Arbouet, D. Christofilos, N. Del Fatti, F. Vallée, J. R. Huntzinger, L. Arnaud, P. Billaud, and M. Broyer, "Direct measurement of the single-metal-cluster optical absorption," Phys. Rev. Lett. **93**, 127401 (2004).
[9]O. L. Muskens, P. Billaud, M. Broyer, N. Del Fatti, and F. Vallée, "Optical extinction spectrum of a single metal nanoparticle: Quantitative characterization of a particle and of its local environment," Phys. Rev. B **78**, 205410 (2008).
[10]P. Stoller, V. Jacobsen, and V. Sandoghdar, "Measurement of the complex dielectric constant of a single gold nanoparticle," Opt. Lett. **31**, 2474 (2006).
[11]S. Khadir, D. Andrén, P. C. Chaumet, S. Monneret, N. Bonod, M. Käll, A. Sentenac, and G. Baffou, "Full optical characterization of single nanoparticles using quantitative phase imaging," Optica **7**, 243–248 (2020).
[12]P. B. Johnson and R. W. Christy, "Optical constants of noble metals," Phys. Rev. B **6**, 4370–4379 (1972).
[13]K. M. McPeak, S. V. Jayanti, S. J. P. Kress, S. Meyer, S. Iotti, A. Rossinelli, and D. J. Norris, "Plasmonic films can easily be better: Rules and recipes," ACS Photon. **2**, 326–333 (2015).
[14]N. A. Mortensen, S. Raza, M. Wubs, T. Søndergaard, and S. I. Bozhevolnyi, "A generalized non-local optical response theory for plasmonic nanostructures," Nat. Commun. **5**, 4809 (2014).
[15]T. Christensen, W. Yan, A.-P. Jauho, M. Soljačić, and N. A. Mortensen, "Quantum corrections in nanoplasmonics: Shape, scale, and material," Phys. Rev. Lett. **118**, 157402 (2017).
[16]D. Gall, "Electron mean free path in elemental metals," J. Appl. Phys. **119**, 085101 (2016).
[17]C. Voisin, N. D. Fatti, D. Christofilos, and F. Vallée, "Ultrafast electron dynamics and optical nonlinearities in metal nanoparticles," J. Phys. Chem. B **105**, 2264–2280 (2001).
[18]B. Foerster, A. Joplin, K. Kaefer, S. Celiksoy, S. Link, and C. Sönnichsen, "Chemical interface damping depends on electrons reaching the surface," ACS Nano **11**, 2886–2893 (2017).
[19]L. M. Payne, W. Albrecht, W. Langbein, and P. Borri, "The optical nanosizer – quantitative size and shape analysis of individual nanoparticles by high-throughput widefield extinction microscopy," Nanoscale **12**, 16215–16228 (2020).
[20]F. Masia, W. Langbein, and P. Borri, "Measurement of the dynamics of plasmons inside individual gold nanoparticles using a femtosecond phase-resolved microscope," Phys. Rev. B **85**, 235403 (2012).
[21]M. Guerrisi, R. Rosei, and P. Winsemius, "Splitting of the interband absorption edge in au," Phys. Rev. B **12**, 557–563 (1975).
[22]C. Voisin, D. Christofilos, P. A. Loukakos, N. D. Fatti, F. Vallée, J. Lermé, M. Gaudry, E. Cottancin, M. Pellarin, and M. Broyer, "Ultrafast electron-electron scattering and energy exchanges in noble-metal nanoparticles," Phys. Rev. B **69**, 195416 (2004).
[23]L. M. Payne, W. Langbein, and P. Borri, "Wide-field imaging of single-nanoparticle extinction with sub-nm^2 sensitivity," Phys. Rev. Appl **9**, 034006 (2018).
[24]T. Moon, "The expectation-maximization algorithm," IEEE Signal Processing Magazine **13**, 47–60 (1996).
[25]W. van Aarle, W. J. Palenstijn, J. D. Beenhouwer, T. Altantzis, S. Bals, K. J. Batenburg, and J. Sijbers, "The ASTRA toolbox: A platform for advanced algorithm development in electron tomography," Ultramicroscopy **157**, 35–47 (2015).

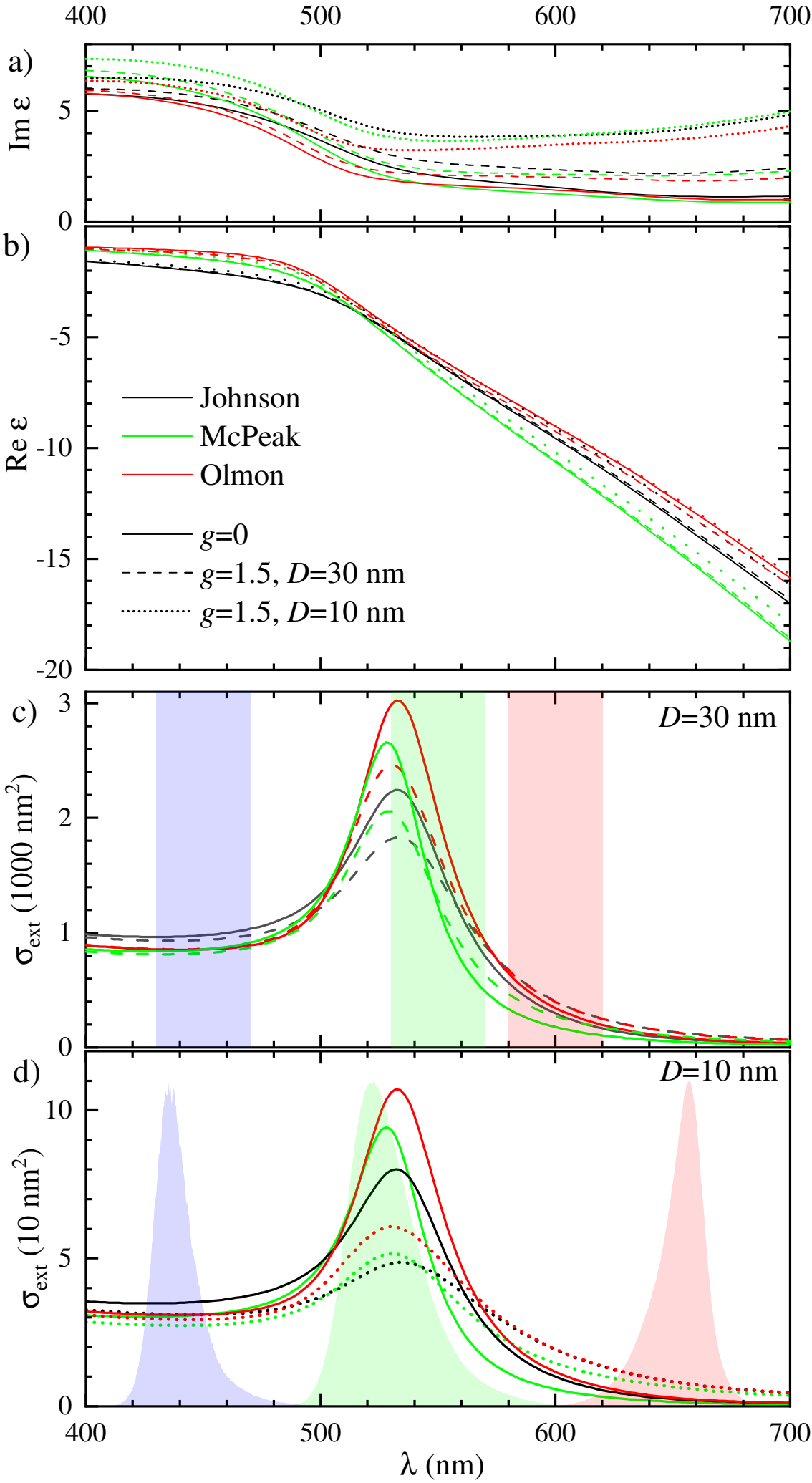
a)
Im ε
b)
Re ε
Johnson
McPeak
Olmon
g=0
g=1.5, D=30 nm
g=1.5, D=10 nm
c)
D=30 nm
σext (1000 nm2)
d)
D=10 nm
σext (10 nm2)
λ (nm)

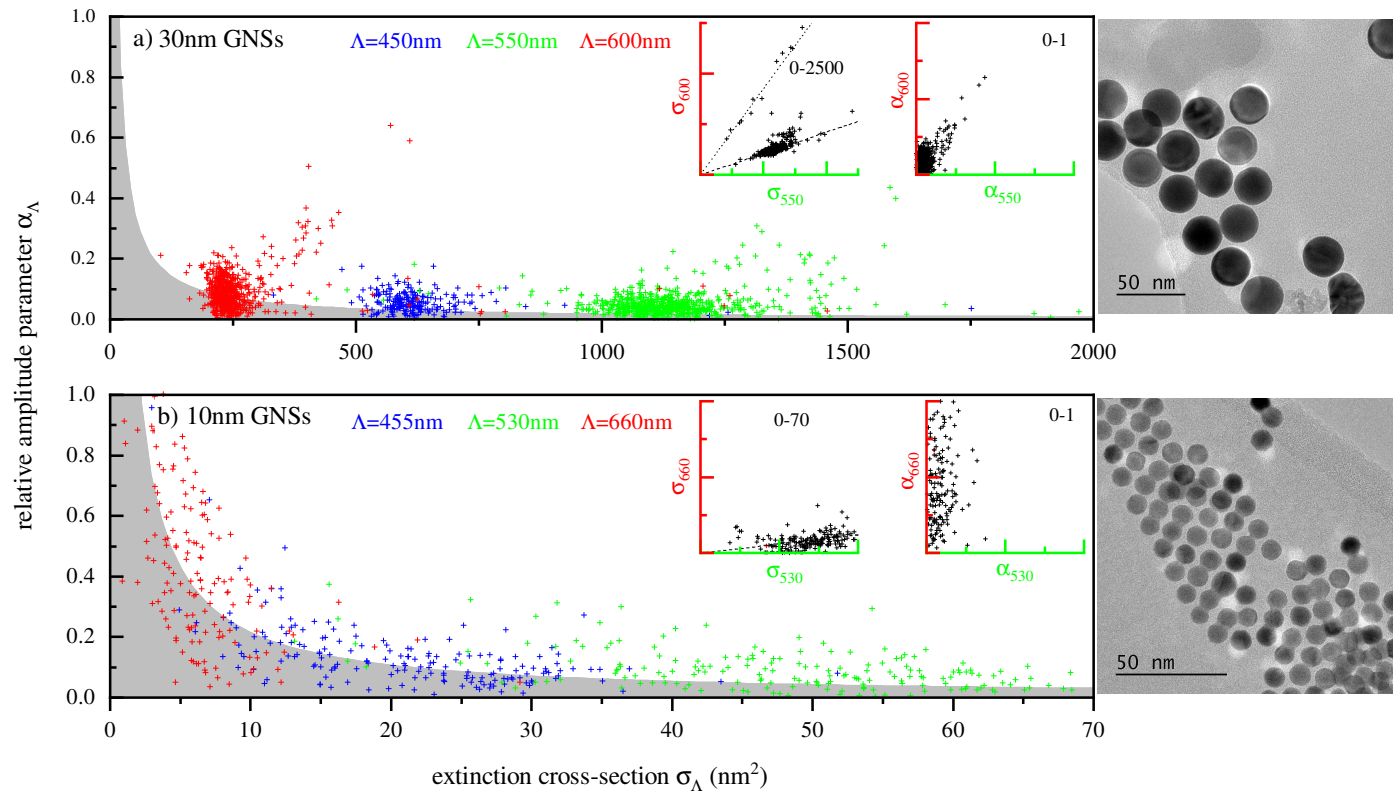
a) 30nm GNSs
Λ=450nm
Λ=550nm
Λ=600nm
0-2500
σ600
σ550
0-1
α600
α550
50 nm
b) 10nm GNSs
Λ=455nm
Λ=530nm
Λ=660nm
0-70
σ660
σ530
0-1
α660
α530
50 nm
relative amplitude parameter αΛ
extinction cross-section σΛ (nm2)

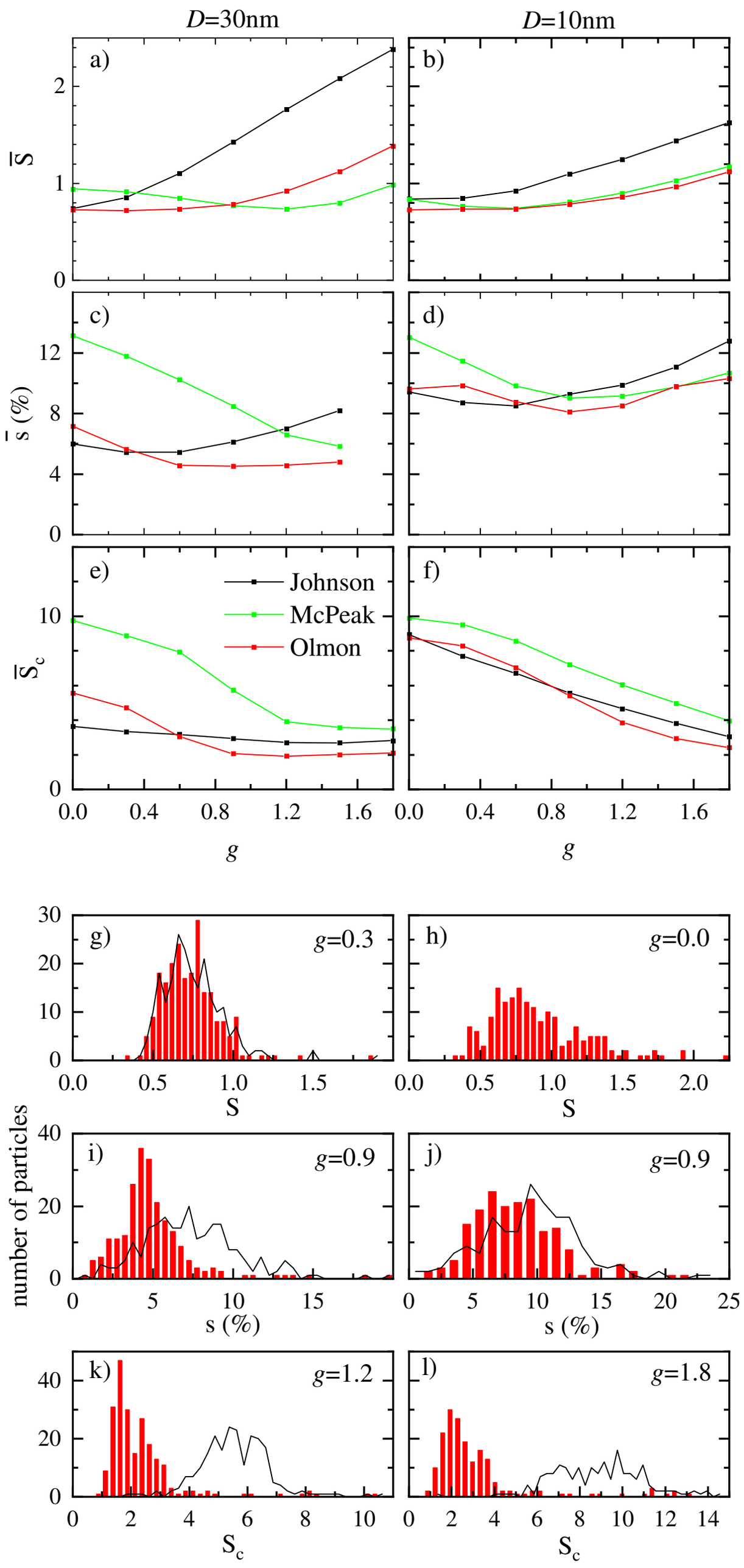
D=30nm
D=10nm
a)
b)
c)
d)
e)
f)
g)
h)
i)
j)
k)
l)
Johnson
McPeak
Olmon
g=0.3
g=0.0
g=0.9
g=0.9
g=1.2
g=1.8
g
g
S
S
s (%)
s (%)
S_c
S_c
number of particles

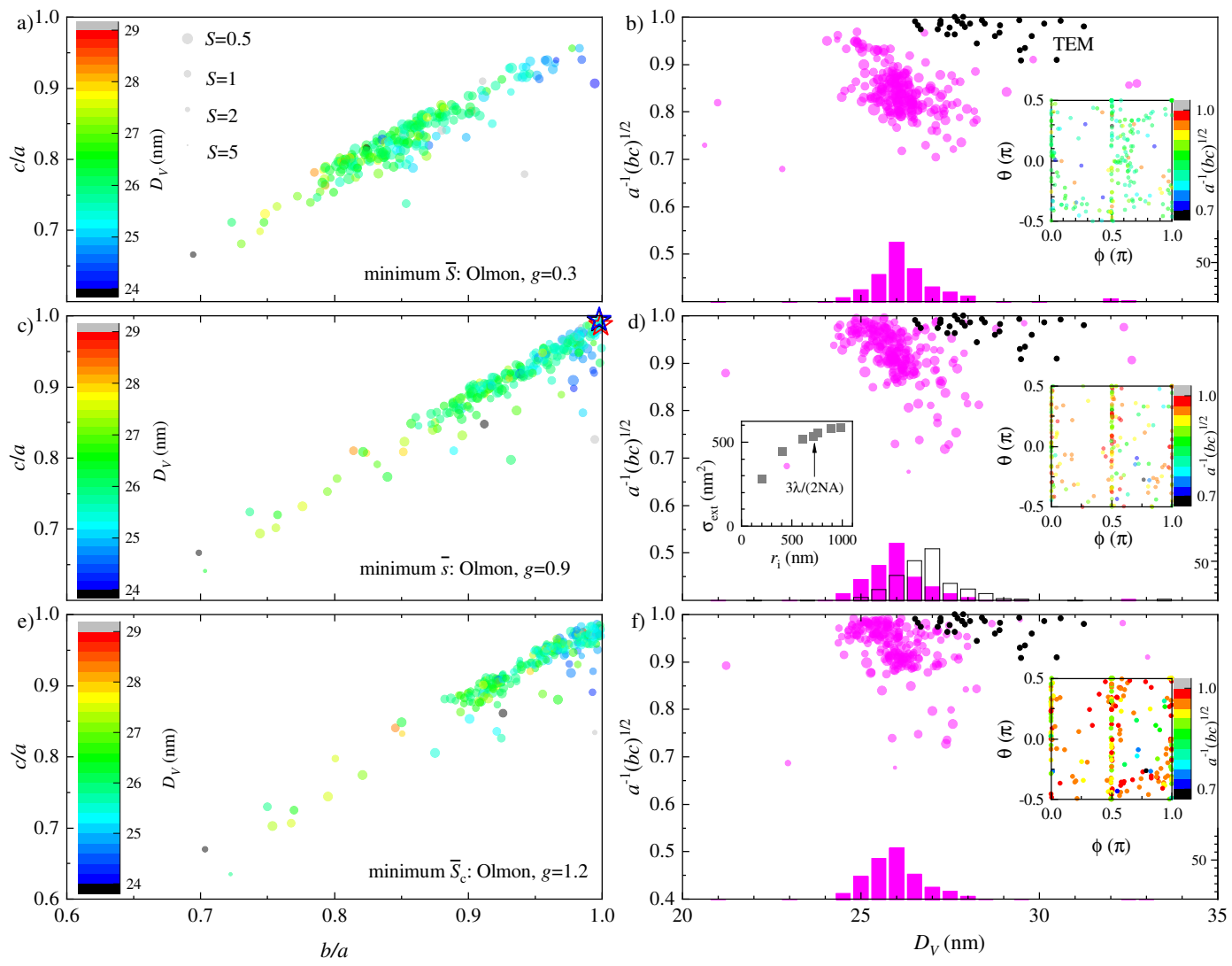
a)
b)
c)
d)
e)
f)
TEM
S=0.5
S=1
S=2
S=5
minimum $\bar{S}$: Olmon, g=0.3
minimum $\bar{s}$: Olmon, g=0.9
minimum $\bar{S}_c$: Olmon, g=1.2
3λ/(2NA)
c/a
b/a
D_V (nm)
$a^{-1}(bc)^{1/2}$
θ (π)
ϕ (π)
σ_{ext} (nm^2)
r_i (nm)

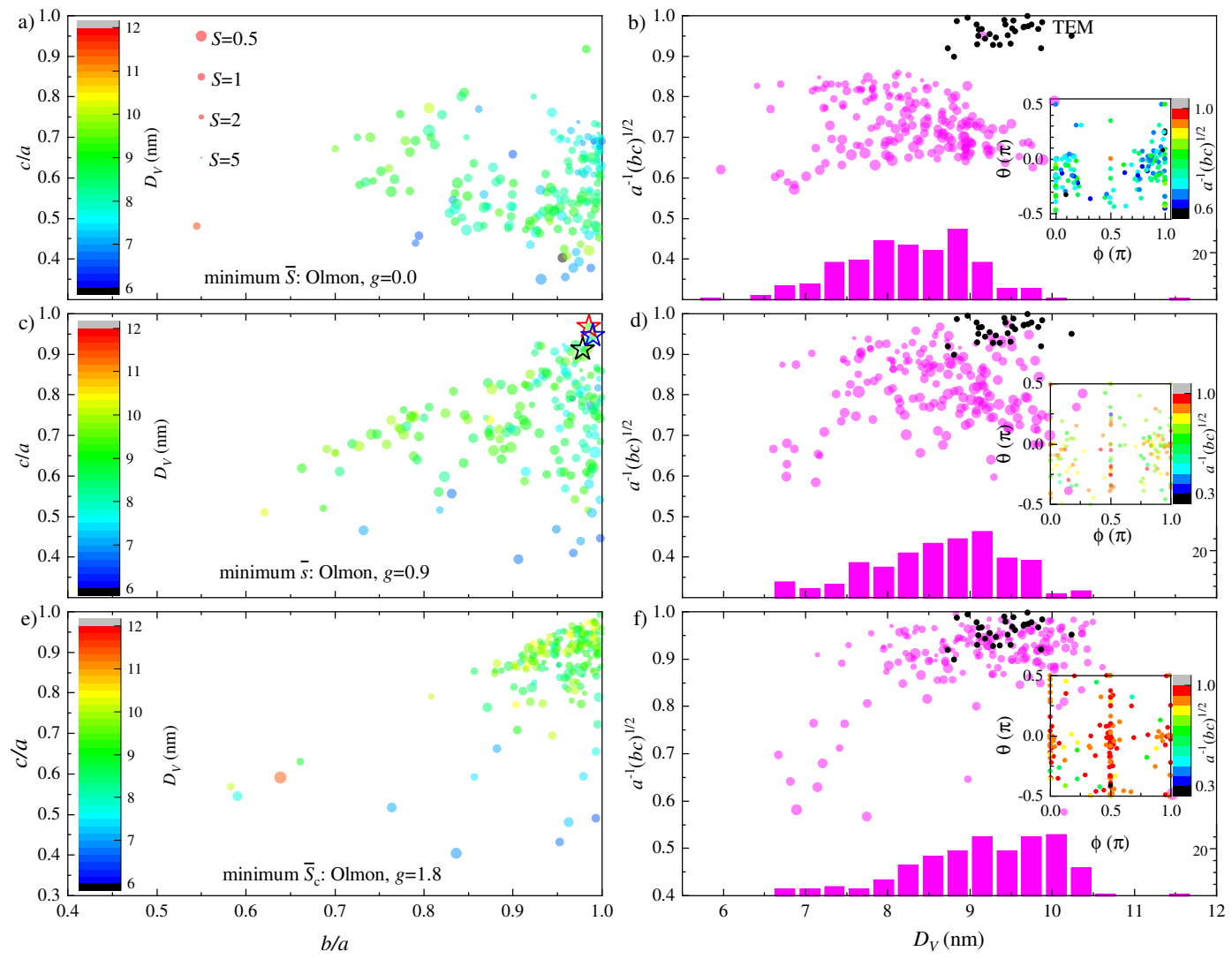
a)
b)
c)
d)
e)
f)
TEM
S=0.5
S=1
S=2
S=5
minimum $\bar{S}$: Olmon, g=0.0
minimum $\bar{s}$: Olmon, g=0.9
minimum $\bar{S}_c$: Olmon, g=1.8
c/a
b/a
D_V (nm)
$a^{-1}(bc)^{1/2}$
θ (π)
ϕ (π)

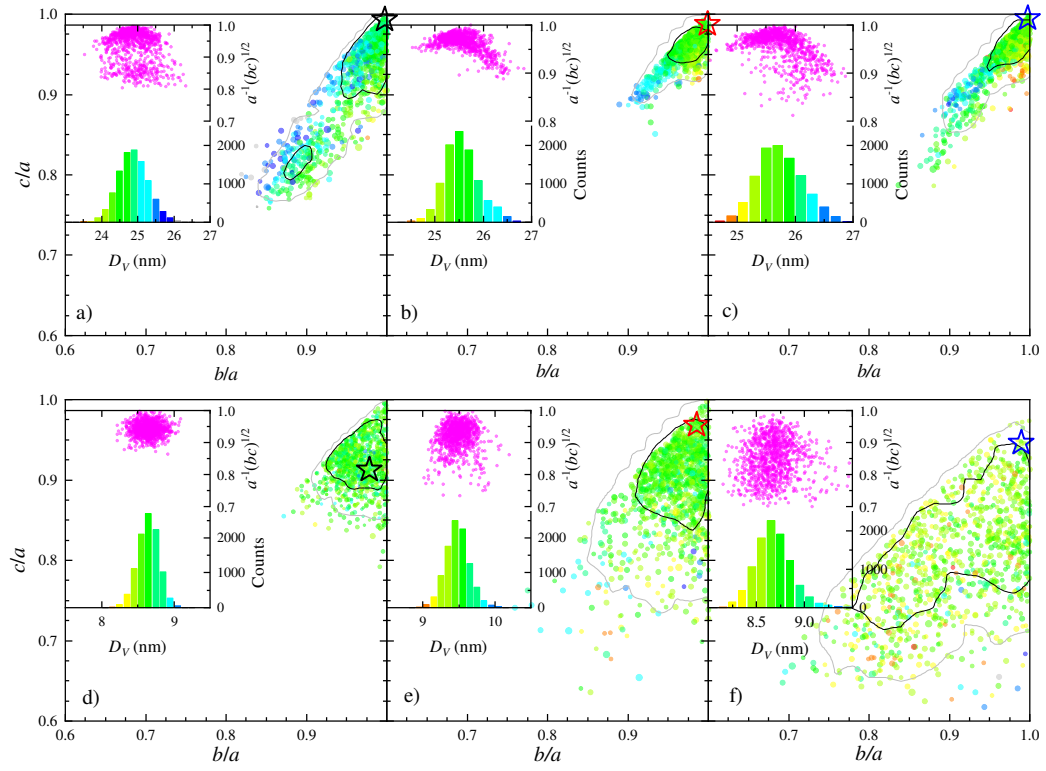
a)
b)
c)
d)
e)
f)
c/a
b/a
$a^{-1}(bc)^{1/2}$
D_V (nm)
Counts

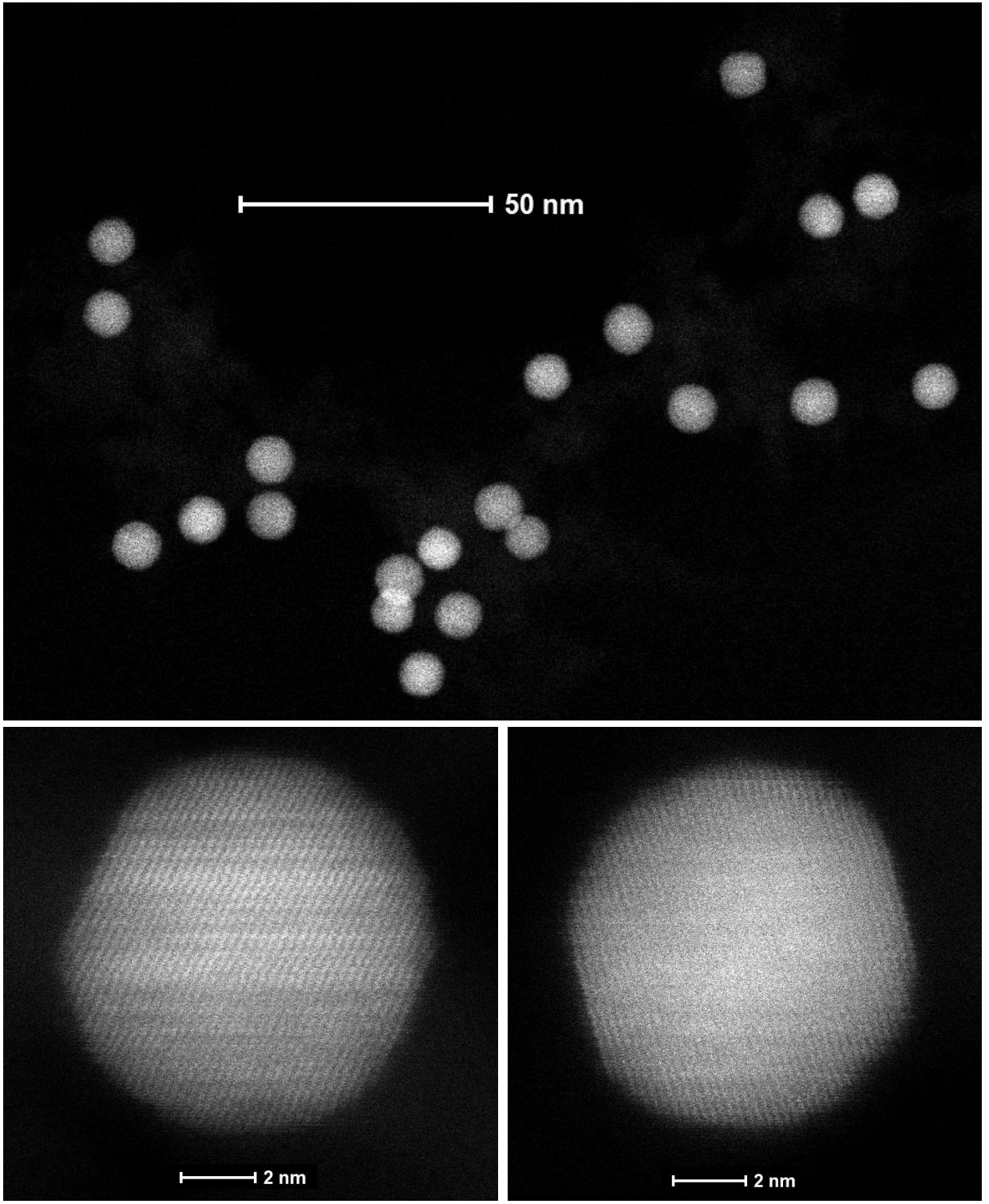
50 nm
2 nm
2 nm

30nm

1

2

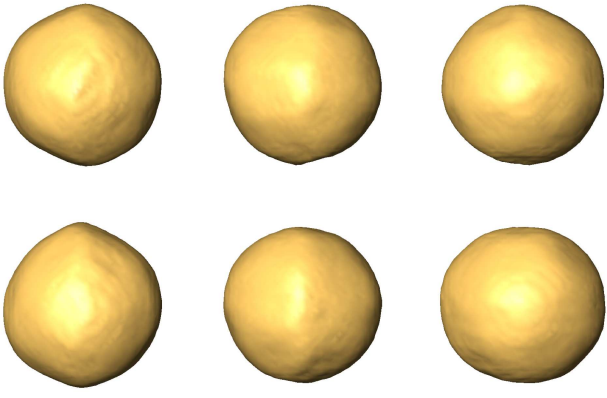

10nm

1

2

3